

14

AD-A230 269

DTIC FILE COPY

Annual Letter Report

Growth, Nitrogen Vacancy Reduction and Solid Solution Formation in Cubic GaN Thin Films and the Subsequent Fabrication of Superlattice Structures Using AlN and InN

Supported under Grant #N00014-86-K-0686 P5
Innovative Science and Technology Office
of the Strategic Defense Initiative
Office of the Chief of Naval Research
Report for the period January 1, 1990–December 31, 1990

DTIC
SELECTED
DEC 28 1990
S D

Robert F. Davis, Michael J. Paisley and Zlatko Sitar
Materials Science and Engineering Department
North Carolina State University
Campus Box 7907
Raleigh, NC 27695-7907

DISTRIBUTION STATEMENT
UNCLASSIFIED
EXCEPT WHERE SHOWN
OTHERWISE

December, 1990

00 230 269

REPORT DOCUMENTATION PAGE

Form Approved
OMB No 0704-0188

Public reporting burden for this collection of information is estimated to average 1 hour per response, including the time for reviewing instructions, searching existing data sources, gathering and maintaining the data needed, and completing and reviewing the collection of information. Send comments regarding this burden estimate or any other aspect of this collection of information, including suggestions for reducing this burden to Washington Headquarters Services, Directorate for Information Operations and Reports, 1215 Jefferson Davis Highway, Suite 1204, Arlington, VA 22202-4302 and to the Office of Management and Budget, Paperwork Reduction Project (0704-0188), Washington, DC 20503

| | | | | |
|---|---|--|--|--|
| 1. AGENCY USE ONLY (Leave blank) | | 2. REPORT DATE December, 1990 | 3. REPORT TYPE AND DATES COVERED Annual Letter 1/1/90-12/31/90 | |
| 4. TITLE AND SUBTITLE Growth, Nitrogen Vacancy Reduction and Solid Solution Formation in Cubic GaN Thin Films and the Subsequent Fabrication of Superlattice Structures Using AlN and InN | | | 5. FUNDING NUMBERS R&T:s400001srq05 S.O.:1114SS | |
| 6. AUTHOR(S) Robert F. Davis | | | | |
| 7. PERFORMING ORGANIZATION NAME(S) AND ADDRESS(ES) North Carolina State University Hillsborough Street Raleigh, NC 27695 | | | 8. PERFORMING ORGANIZATION REPORT NUMBER N00014-86-K-0686 P5 | |
| 9. SPONSORING/MONITORING AGENCY NAME(S) AND ADDRESS(ES) Sponsoring: ONR, 800 N. Quincy, Arlington, VA 22217 Monitoring: Office of Naval Research Resider, N66005 The Ohio State University Research Center 1314 Kinnear Road Columbus, OH 43212-1194 | | | 10. SPONSORING/MONITORING AGENCY REPORT NUMBER | |
| 11. SUPPLEMENTARY NOTES | | | | |
| 12a. DISTRIBUTION/AVAILABILITY STATEMENT Approved for Public Release; Distribution Unlimited | | | 12b. DISTRIBUTION CODE | |
| 13. ABSTRACT (Maximum 200 words) In the research of this reporting period, AlN films and AlN/GaN layered structures have been grown and structurally, chemically and optically characterized. In addition, BN has been similarly deposited on cubic (β)-SiC and diamond substrates. Strained layer superlattices have been fabricated for the first time between GaN and AlN. The energy offset was up to 260 meV for the superlattices with the thinnest barriers. A system for atomic layer epitaxy of GaN and AlN has been designed and is under construction. Cubic BN was deposited on the aforementioned substrates; however, significant carbon was also present. The latter problem has now been resolved. Laser ablation of hexagonal BN was also studied; however, only amorphous, wurtzite and hexagonal (graphitic) BN was detected in the films. < | | | | |
| 14. SUBJECT TERMS gallium nitride, aluminum nitride, boron nitride, atomic layer epitaxy, layered structures, transmission electron microscopy, photoluminescence, gas-source MBE, laser ablation, borazine | | | 15. NUMBER OF PAGES 57 | |
| | | | 16. PRICE CODE | |
| 17. SECURITY CLASSIFICATION OF REPORT UNCLAS | 18. SECURITY CLASSIFICATION OF THIS PAGE UNCLAS | 19. SECURITY CLASSIFICATION OF ABSTRACT UNCLAS | 20. LIMITATION OF ABSTRACT SAR | |

Table of Contents

| | |
|--|-----------|
| I. AlN/GaN Superlattices Grown by Gas Source Molecular Beam Epitaxy | 1 |
| A. Introduction | 1 |
| B. Experimental Procedures | 1 |
| C. Experimental Results | 3 |
| 1. Chemical Analysis | 3 |
| 2. Structural and Microstructural Analyses | 4 |
| X-ray Analysis | 4 |
| Transmission Electron Microscopy | 6 |
| 3. Optical Characterization | 3 |
| D. Summary | 13 |
| II. Luminescence and Lattice Parameter of Cubic Gallium Nitride | 14 |
| A. Introduction | 14 |
| B. Experimental Procedure | 15 |
| C. Experimental Results | 15 |
| D. Summary | 18 |
| III. The Effect of Electron Beam Irradiation on Mg Doped GaN Thin Films | 19 |
| A. Introduction | 19 |
| B. Experimental Procedure | 19 |
| C. Results and Discussion | 21 |
| D. Summary | 24 |
| IV. Atomic Layer Epitaxy of GaN and AlN | 24 |
| A. Introduction | 24 |
| B. The ALE System | 25 |
| V. Future Research in GaN and AlN | 28 |
| VI. Growth of Boron Nitride Films via Gas-Source MBE | 28 |
| A. Introduction | 28 |
| B. Boron Nitride on Silicon Carbide | 29 |
| Overview | 29 |
| Chemical Analysis | 30 |
| Structural Analysis | 32 |
| C. Boron Nitride on Diamond (100) | 34 |
| D. Boron Nitride on Silicon (100) | 38 |
| Overview | 38 |
| Chemical Analysis | 40 |
| Structural and Microstructural Analyses | 41 |
| VII. Growth of Boron Nitride Films via Laser Ablation | 46 |

| | |
|---|----|
| VIII. Characterization of Sumitomo c-BN | 49 |
| IX. Future Research in the Growth of BN Films | 51 |
| A. Gas Source MBE | 51 |
| B. Laser Ablation | 51 |
| C. Analytical Techniques | 52 |
| X. References | 52 |



| | |
|---------------------|-------------------------------------|
| Accession For | |
| NTIS CRA&I | <input checked="" type="checkbox"/> |
| DTIC TAB | <input type="checkbox"/> |
| Unannounced | <input type="checkbox"/> |
| Justification | |
| By | |
| Distribution/ | |
| Availability Codes | |
| Dist | Avail and/or Special |
| A-1 | |

I. AlN/GaN Superlattices Grown by Gas Source Molecular Beam Epitaxy

A. Introduction

Commercialization of light emitting optoelectronic devices in the previous decade stimulated considerable interest in those III-V nitrides which possess a direct energy gap in the UV region of the spectrum. A comprehensive review regarding the thin film and optoelectronic research in GaN prior to 1988 has recently been published [1]. Depositions of AlN and AlGa_N have also been studied [2,3].

Bandgap engineering in the range of 3.4–6.2 eV can be achieved either by solid solutions or by superlattices of GaN and AlN. The latter are favored for several reasons. As has been shown for the GaAs/GaAlAs system [4,7], optoelectronic devices using multi-quantum well structures instead of heterostructures exhibit lower threshold current density, lower non-radiative recombination rate, narrower emission spectra and reduced sensitivity to temperature. The lattice parameter mismatch between AlN and GaN is only 2.5%, thus layered structures of these two materials offer a way of producing high quality, low dislocation density GaN- and/or AlN-based materials and devices. To our knowledge, superlattices of these two materials (or any other wurtzite semiconductor) have not been produced prior to this investigation. These are also the first semiconducting superlattices exhibiting band discontinuity well above 1 eV.

The following sections describe the procedures used to deposit and characterize the layered structures as well as detail the results and conclusions of this research.

B. Experimental Procedures

The growth system was a modified Perkin-Elmer 430 MBE system. Standard effusion cells were used for the evaporation of Ga and Al, while the nitrogen was activated in a small, MBE compatible, ECR plasma source [8].

The growth studies were conducted on (0001)-oriented a-SiC (6H polytype) and (0001) oriented epitaxial quality sapphire substrates, both of which have a hexagonal structure. All substrates were chemically cleaned and thermally desorbed in the vacuum at 900°C prior to the introduction in the growth chamber. All superlattices were grown under the same conditions, which are summarized in Table I.

TABLE I. Experimental conditions for the deposition of GaN and AlN by gas-source MBE

| | |
|---|------------------------------|
| Nitrogen pressure | 1×10^{-4} Torr |
| Nitrogen flow rate | 4–5 sccm |
| Microwave power | 50 W |
| Nitrogen ion current density at the substrate | 150–200 μAcm^{-2} |
| Substrate temperature | 600°C |
| Growth rate: | |
| GaN | ≈ 2.5 nm/min |
| AlN | ≈ 1.6 nm/min |
| GaN buffer layer thickness | 140 nm |
| Period thickness | 1.5–40 nm |
| Number of periods | 20–200 |
| Total growth time | 6–7 hrs |

Scanning Auger microprobe (SAM) (JEOL JAMP-30) analysis was used to determine the presence of impurities and the nominal compositions of the AlN and GaN layers. The superlattices were subsequently analyzed by x-ray diffractometry using $\text{CuK}\alpha$ to determine layer period and the crystalline quality of the films. Transmission electron microscopy (TEM) (Hitachi H-800) and high resolution microscopy (HREM) (JEOL 200CX) were used for further analysis. Cross-sectional TEM specimens were prepared using standard techniques [9]. The luminescent properties of the samples grown on a(6H)-SiC were examined by cathodoluminescence. The spectra were taken at 77 K in the wavelength range of 200 to 800 nm using the excitation electron beam energies of 7 keV.

C. Experimental Results

1. Chemical Analysis

Figure 1 shows an Auger depth profile taken from a sample with 20 AlN/GaN double layers. The layers of each material were 10 nm thick. The profile indicates well defined layers. The spectra indicate nominal AlN and GaN compositions and some mixing of Ga and Al in the AlN and GaN layers, respectively. A small amount of interfacial mixing may be present; however, the Auger data exaggerate this phenomenon because of insufficient depth resolution. This resolution in the sputter Auger technique depends on the escape depth of the Auger electrons (≈ 5 nm) and the depth resolution of the sputtering process (also ≈ 5 nm). For both reasons was the instrument's depth resolution in this study in the same range as the layer thickness. The fact that the Auger depth profiling exaggerates interlayer mixing for very thin layers can be proven by examination of the TEM results (see below) which show well defined layers even at a thickness of only two monolayers.

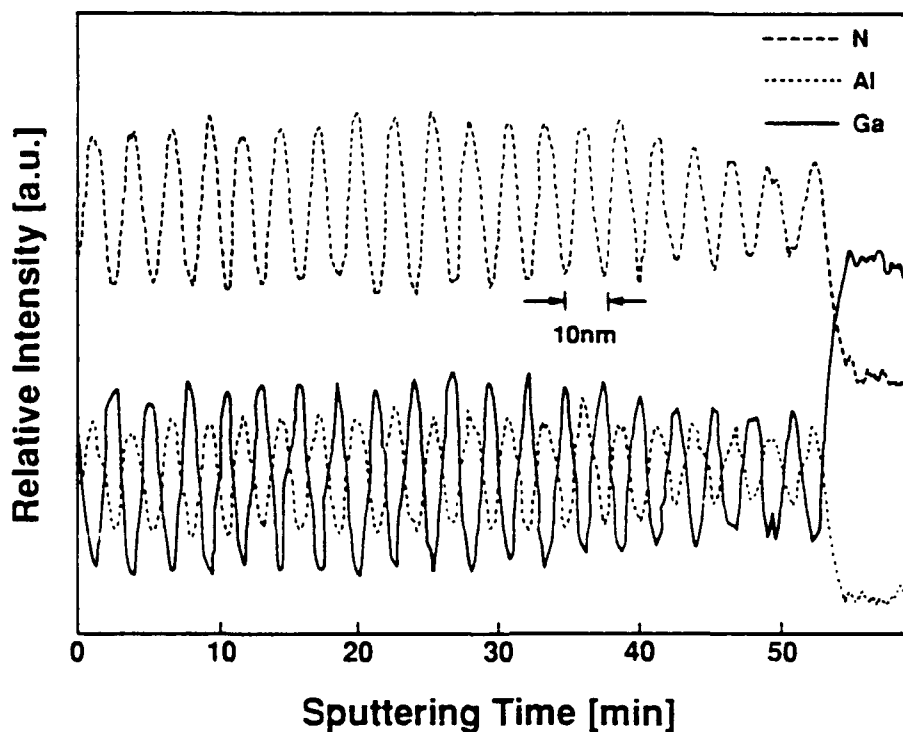


Figure 1. Auger depth profile taken from a sample with 20 AlN/GaN double layers. The layers of each material were 10 nm thick.

2. Structural and Microstructural Analyses

X-ray Analysis. Figures 2(a1–a3) show the evolution of the diffraction peaks as a function of decreasing AlN/GaN bilayer periodicity, P , which is given as:

$$P = t_{\text{AlN}} + t_{\text{GaN}} , \quad (1)$$

where t_{AlN} and t_{GaN} are the respective thicknesses of the individual layers of AlN and GaN. Each spectrum shows the (0002) diffraction peak from the GaN buffer layer, the zero order superlattice peak (marked "0") which represents the average vertical lattice parameter of the superlattice and the associated satellite peaks (marked from -4 to 3). The fact that the GaN and the zeroth-order superlattice peaks do not coincide shows that the superlattices are sufficiently thick to be structurally independent of the GaN buffer layer. As such, the lattice constant in the structure is characteristic of the superlattice rather than the substrate. The biaxial strain is shared between the GaN and the AlN layers, as the GaN layers are biaxially compressed and the AlN layers are biaxially dilated.

Since the buffer layer peak is superimposed on the superlattice peaks, it makes the diffraction from the superlattice unclear. As such, each spectrum in Figures 2(a1–a3) was fitted with a sum of Lorentzian peaks followed by the subtraction of both the buffer layer peak and the overall background. This allows the evolution of the peaks with the change in superlattice period to be more easily observed. The resulting spectra are shown in Figures 2(b1–b3). In this latter set of spectra, the x-ray intensities are plotted as a function of $2/c$, where c is the lattice parameter perpendicular to the superlattice. This is convenient for measuring the parameters P , t_{AlN} , t_{GaN} , c_{GaN} , and c_{AlN} directly from the spectra. A representative diffraction spectrum having marked parameters characteristic of a superlattice produced in this study is shown in Figure 2(b1).

Figure 2 (b1) shows two almost completely separated sets of superlattice peaks, each of which represents one of the two materials. The center of the GaN

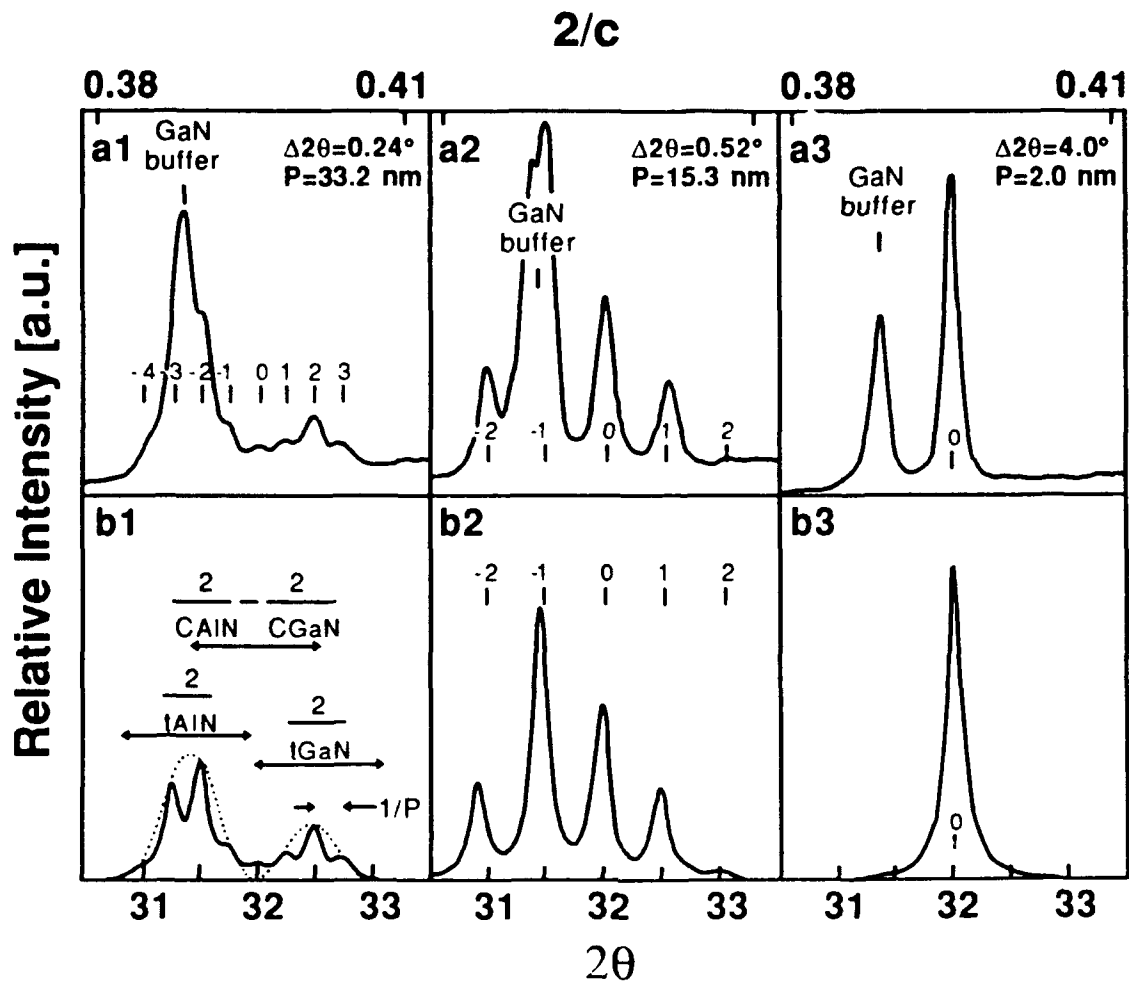


Figure 2. (a) X-ray diffraction spectra of the samples with different periodicities. Each pattern is characterized by the (0002) peak from the GaN buffer layer (marked by "GaN buffer") and a zero-order peak from AlN/GaN layers at $2\theta = 32^\circ$ (marked by "0") with satellite peaks around it. An angular spacing, $\Delta 2\theta$, of satellite peaks and a calculated bilayer period, P , is given for each spectrum. (b) Diffraction spectra after the subtraction of the GaN buffer layer peak and the overall background. Figure (b1) illustrates the use of the spectra for the determination of different parameters (see text).

envelope coincides with the GaN buffer layer peak. This indicates that both have the same vertical lattice spacings. Since the center of the AlN envelope also appears at the same angular position as one would expect for the (0002) peak of bulk AlN, this indicates that individual layers at this period have unchanged vertical lattice parameters and thus are relaxed with respect to each other.

As the period decreases, the positions of the envelopes change. This is believed to be related to the biaxial lattice distortion due to elastic strain. In Figure 2 (b2) both sets of peaks begin to overlap, and the exact positions of the two envelopes become less obvious. As one moves toward even shorter periods the two envelopes can no longer be resolved. As a consequence of shorter periods the number of observable satellite peaks decreases. Figure 2 (b3), which represents the diffraction spectrum of a superlattice with $P=2$ nm, shows only the zero-order superlattice peak which is located approximately midway between the expected peaks for pure AlN and pure GaN. The peak corresponds to an interplanar spacing of 0.252 nm, which is intermediate between the spacings of the (0002) planes of AlN (0.249 nm) and GaN (0.258 nm) and represents the average spacing of the (0002) planes in the superlattice. Satellite peaks for this sample are out of the range of the scan, and are expected to be at $\approx 28^\circ$ and $\approx 36^\circ$. As noted above, TEM results show a well defined layered structure; thus, there is no reason to believe that this peak arises from the homogeneous mixing of the two materials.

According to the diffraction results, the transition between the relaxed and strained structures occurs at a layer thickness between 6 and 8 nm. This is in good agreement with the calculated value of 7.5 nm as the critical thickness using the method of Matthews and Blakeslee [10]. In order to more accurately determine the critical thickness, the reflections from the planes with mixed indices (for example $(10\bar{1}1)$) should be studied.

Transmission Electron Microscopy. The periodicities calculated from the x-ray spectra were confirmed by the TEM images. Discrepancies between the two methods were found to be less than 5%.

Figure 3 shows a TEM image of 20 nm thick layers of AlN and GaN grown on (0001) a(6H)-SiC. GaN layers are dark and those of AlN are light. Layers are well

defined and have few structural defects. The $(01\bar{1}0)$ diffraction pattern (inset), taken from the layered structure, confirms the monocrystalline nature of the film.

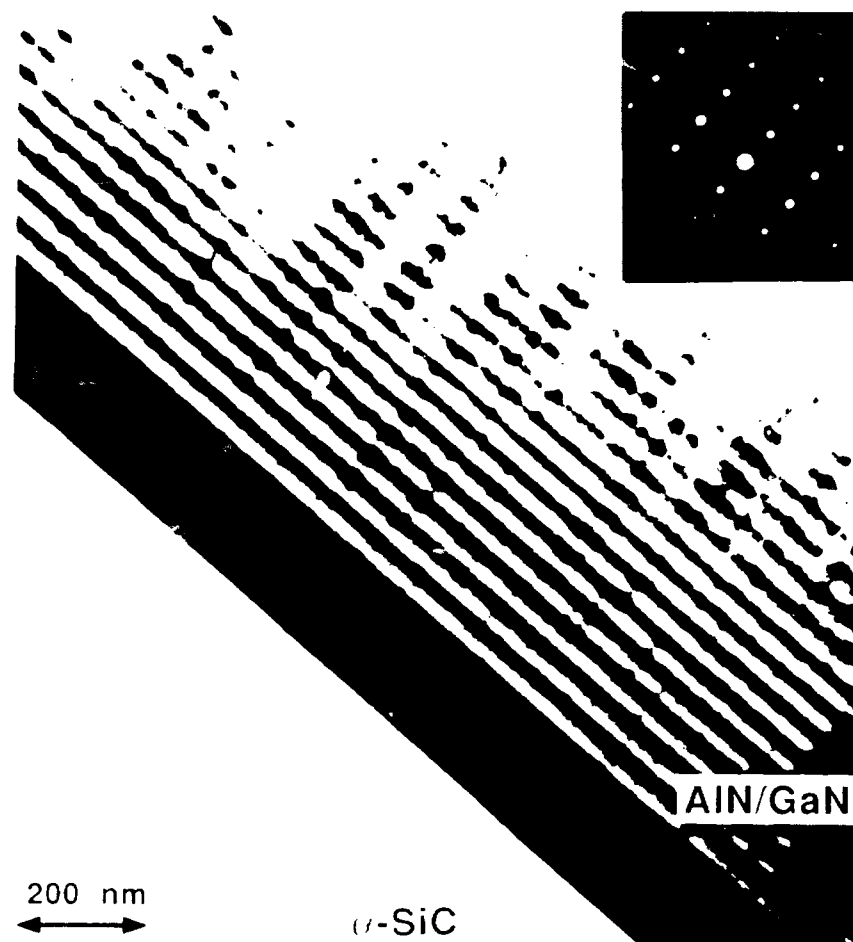


Figure 3. AlN/GaN superlattices grown on α (6H)-SiC. The thickness of the individual layers is 20 nm. Inset shows an electron diffraction pattern of this superlattice (zone axis $(01\bar{1}0)$), which confirms the crystalline quality.

By contrast, structures grown on sapphire showed a columnar structure with slight misorientation. However, layers of the two materials within individual crystallites are well defined, and no misfit dislocations or other defects have been found for layers thinner than 7 nm. Even the structure containing 0.5 nm thick AlN layers (2 monolayers) and 1 nm thick GaN layers (4 monolayers), shown in Figure 4, show very good compositional contrast.

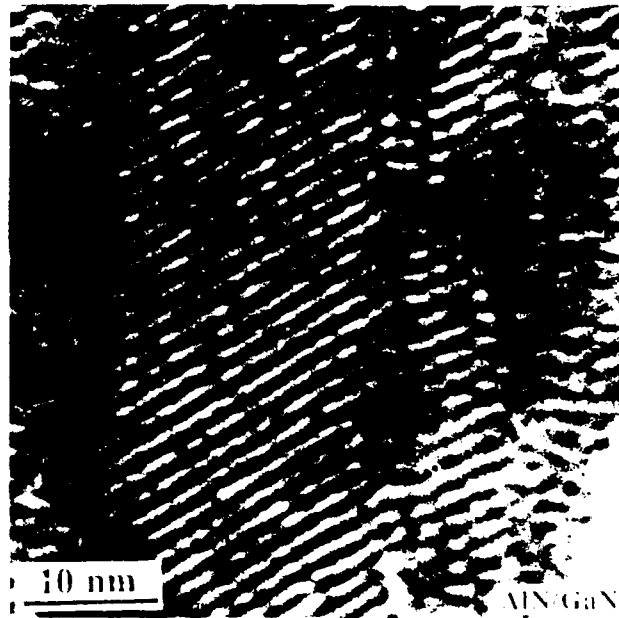


Figure 4. AlN/GaN superlattice grown on sapphire. The thickness of AlN and GaN layers is 0.5 nm and 1 nm, respectively.

3. Optical Characterization

The bandgap difference between AlN and GaN is 2.8 eV. Thus layers of these two materials produce almost one order of magnitude larger band discontinuities than are achieved in AlGaAs or InGaAs systems. As such, AlN/GaN superlattices may provide some interesting insights regarding the behavior of electrons and holes. For example, they have the potential of providing several well-separated confined electronic states.

Two different cases were examined: 1) the emission energy shift as a function of the layer thickness with the thicknesses of the GaN and AlN layers maintained equal (i. e. $t_{\text{AlN}} = t_{\text{GaN}} = \frac{P}{2}$) and 2) the emission energy shift as a function of the barrier (AlN) thickness, while the well (GaN) thickness was maintained constant at 1 nm.

The allowed energy bands for the electrons in the conduction band and for the holes in the valence band in the superlattice were calculated using a one-dimensional

Krönig-Penney model [11]. According to this model an electron or a hole can occupy a particular energy state in the superlattice only if the following is true:

$$1 \geq \left| \cos \left[\frac{t_1(2mE)^{\frac{1}{2}}}{\hbar} \right] \cosh \left[\frac{t_2(2m(V-E))^{\frac{1}{2}}}{\hbar} \right] + \left(\frac{V}{E} - 1 \right)^{\frac{1}{2}} \left(\frac{V}{2E} - 1 \right) \sin \left[\frac{t_1(2mE)^{\frac{1}{2}}}{\hbar} \right] \sinh \left[\frac{t_2(2m(V-E))^{\frac{1}{2}}}{\hbar} \right] \right|$$

In this expression is E the energy of the electrons (holes), V the barrier height (band discontinuity), m the effective mass of the carriers, \hbar is Planck's constant divided by 2π , and t_1 and t_2 are the well and barrier widths, respectively. Since there are no accepted values for the effective masses of the electrons and holes in either AlN or GaN, the average values of the available data were used [12]. The effective mass of the electrons was taken as $0.2m_0$ and that of the holes as $0.8m_0$.

A conduction and valence band discontinuity was determined by iteration to provide the best fit to the transition energies observed by cathodoluminescence. The best fit was obtained when one half of the total bandgap discontinuity (1.4 eV) was assigned to the conduction band and one half to the valence band. The total bandgap discontinuity was calculated as the difference between the bandgaps of AlN and GaN. Because of the lack of data on the mechanical properties of semiconducting nitrides, the effect of the biaxial strain on the bandgap shift could not be included in the calculation, although it is expected to have a considerable influence on the bandgap of both materials.

The shaded areas in Figure 5(a) represent the lowest four calculated energy bands for the electrons in the conduction band and the holes in the valence band as a function of the individual layer thickness. The thicknesses of the AlN and GaN were considered equal in these calculations. The lowest transition energy in the superlattice at a particular layer thickness is obtained as the distance between the lower edge of the first energy band for the electrons and the upper edge of the first energy band for

the holes. The arrows indicate the transitions in the structures with 1, 3, and 10 nm thick AlN and GaN layers. The different lengths of the arrows correspond to the emission energies observed by cathodoluminescence. The luminescence spectra for these three structures are shown in Figure 5(b). The spectra show sharp and well defined peaks with the energies above the bandgap of GaN. The width of the peaks increases with the layer thickness as the superlattice makes a transition from the pseudomorphic to a relaxed structure. The measured and calculated transition energies for these superlattices are collected in Table II.

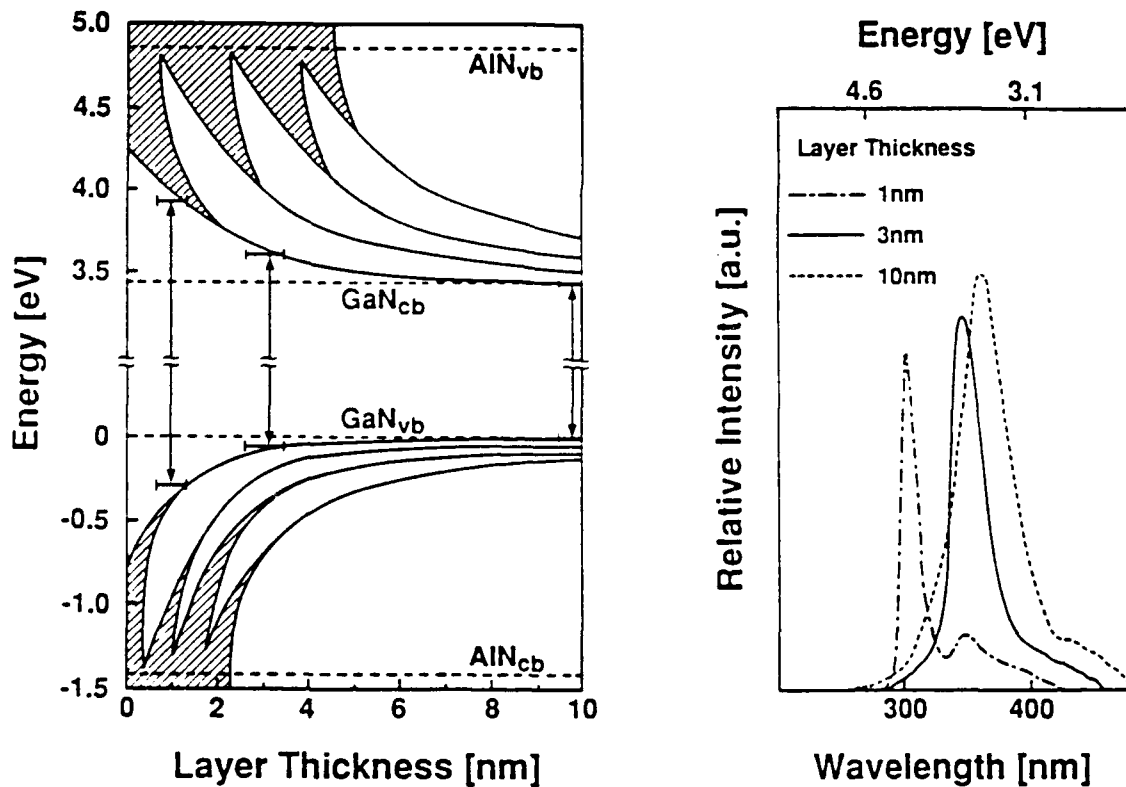


Figure 5. (a) The lowest four calculated energy bands for the electrons in the conduction band and the holes in the valence band as a function of the individual layer thickness while the thicknesses of the AlN and GaN were kept equal. The arrows indicate the transitions in the structures with 1, 3, and 10 nm thick layers, whose cathodoluminescence spectra shown in Figure 5(b).

TABLE II. Calculated and measured transition energies for different layer thicknesses

| Layer thickness [nm] | $E_{\text{calculated}}$ [eV] | E_{measured} [eV] | DE [meV] |
|----------------------|------------------------------|----------------------------|-------------|
| 1 | 4.29 | 4.11 | 180 |
| 3 | 3.64 | 3.47 | 170 |
| 10 | 3.42 | 3.42 | ≈ 0 |

The shaded areas in Figure 6(a) represent the lowest two calculated energy bands for the electrons and the lowest three energy bands for holes as a function of the barrier width at a constant well width of 1 nm. The arrows again indicate the measured transition energy of a particular structure. The measured luminescence spectra for 0.5 nm and 1 nm thick barriers are shown in Figure 6(b). The calculated and measured energies are summarized in Table III.

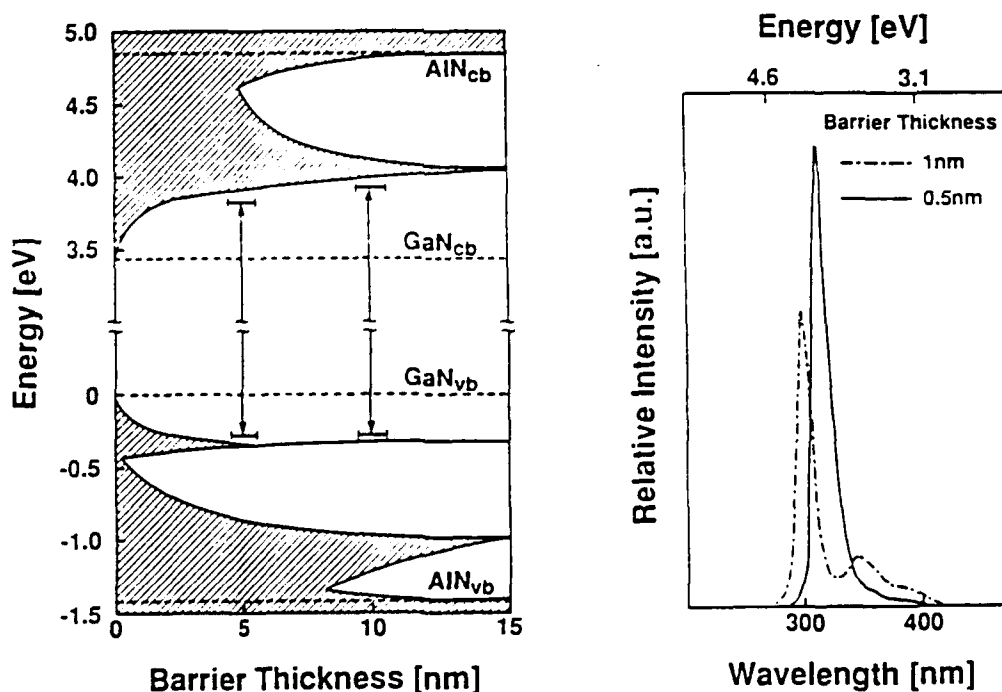


Figure 6: (a) The lowest two energy bands for the electrons and the lowest three energy bands for the holes as a function of the barrier width at a constant well width of 1 nm. The arrows indicate the measured transition energy of a particular structure. The measured luminescence spectra for 0.5 nm and 1 nm thick barriers are shown in Figure 6(b).

TABLE III. Calculated and measured transition energies for different barrier thicknesses.

| Layer thickness [nm] | $E_{\text{calculated}}$ [eV] | E_{measured} [eV] | DE [meV] |
|----------------------|------------------------------|----------------------------|----------|
| 0.5 | 4.19 | 3.93 | 260 |
| 1.0 | 4.29 | 4.11 | 180 |

An examination of both tables reveals the following information: 1) The highest transition energy shift observed in this study was above 700 meV and occurred in the superlattice with 1 nm thick barriers and wells. 2) The emission energy shift for the superlattice with 0.5 nm thick barriers was slightly lower than the previous value because of better coupling between adjacent wells (higher tunneling probability due to thinner barriers). 3) There exists an energy offset between the calculated and measured values, which was in the range of experimental error for 10 nm thick layers and increased to 170 meV for thinner layers and even up to 260 meV for superlattices with the thinnest barriers.

The reasons for the observed offset can be several. 1) There exists a possibility that the values for the effective masses used in the calculation are not accurate. For example if the effective masses were larger, one would obtain lower theoretical values for the transition energies and, as such, a lower offset as well. 2) The lattice mismatch between AlN and GaN produces strain, which induces bandgap shift in both materials. This shift is expected to be rather high for the materials with 2% misfit (i.e., in the range of ≈ 100 meV) [13]. 3) Interfacial mixing of Al in GaN and Ga in AlN in the monolayer scale could significantly change the transition energy in superlattices having individual layers only a few monolayers thick.

The offset for the moderately thin layers (1 and 3 nm) seems to be fairly constant (180 and 170 meV), which would not be the case if only an error in the effective masses were in question. The fact, that the offset is negligible for thick layers

(layers above the critical thickness, which are relaxed with respect to each other) and almost constant for the layers below the critical thickness (which are biaxially strained) implies a connection between the strain induced bandgap shift and the observed offset. As such, the luminescence data could be a rough indicator of whether a layered structure is pseudomorphic or not.

The offset for the superlattices with two monolayer thick barriers is even larger than that of the superlattices with moderately thin individual layers by an additional 90 meV. This jump, which could not be induced by the strain, is most likely the consequence of interfacial mixing, which lowers the barrier height and, as a consequence, causes a decrease in the transition energy. A more sophisticated model, which would include bandgap shift due to elastic strain and also assume one monolayer of interfacial mixing is expected to give much better agreement between the experimental data and theory.

D. Summary

Growth and characterization studies of AlN/GaN layered structures have been conducted using a modified gas source MBE technique. Layers as thin as two monolayers have been grown. X-ray and TEM results revealed strained material (no misfit dislocations at the interfaces) for layers thinner than 6 nm and a completely relaxed structure for layers thicker than 10 nm. Cathodoluminescence studies showed a transition energy shift as high as 700 meV due to the quantum size effect. There exists a constant offset of 170 meV between the experimental and calculated values. Since this offset is present only for the pseudomorphic structures, it has been related to the strain induced bandgap shift of the two materials.

II. Luminescence and Lattice Parameter of Cubic Gallium Nitride

A. Introduction

Because of its wide direct bandgap of 3.45 eV and the large predicted electron drift velocity [14], GaN has the potential for near ultraviolet (NUV) and, with the application of suitable dopants, also for short wavelength visible optoelectronic devices as well as transit-time-limited electronic devices.

The wurtzite (w) polytype of GaN has been grown by numerous investigators using various substrates and deposition techniques. However, the primary limitation of high n-type conductivity and the associated inability to achieve p-type character has been universal in the as-grown films. Pankove [15, 16] speculated, that one might be able to surpass apparently inherent problems of GaN by producing the metastable cubic phase, although there is no fundamental argument for that.

Cubic (c) GaN has been previously reported in the forms of cubic dendrites on the hexagonal phase [17], nearly epitaxial films on (100) GaAs [18], and epitaxial films on (100) b-SiC [19], (0001) sapphire [20], (100) MgO [21] and (100) GaAs [22]. Previously reported values of the lattice parameter a_0 were between 0.450 and 0.455 nm [19-23]. Bandgap and the band structure for cGaN was theoretically predicted by Pankove and Bloom [24]. These calculations used a composite of factors known for hexagonal GaN and for other zinc-blende semiconductors such as GaAs. The resulting value was 3.4 eV, which is essentially that of the hexagonal phase. From the analogy of cubic and hexagonal forms of SiC, which is considered a similar material, one would expect cGaN to have a more narrow forbidden gap than the wurtzite polytype. A considerably lower experimental value of 3.28 and 3.30 has been reported for the room temperature bandgap based on luminescence [25] and absorption [21] measurements, respectively.

B. Experimental Procedure

Cubic GaN thin films were grown by a modified gas source molecular beam epitaxy (MBE) technique in the range of 550-650°C. The precursors were metallic Ga and ultra high purity N₂. A standard effusion cell was used for the evaporation of the Ga, while nitrogen was activated/dissociated in a microwave glow-discharge or in an electron cyclotron resonance (ECR) plasma source [26]. Cubic (zinc blende) β -SiC, (100) orientation, chemically vapor deposited on (100) Si wafers, was used as the substrate. The lattice parameter of β -SiC is 0.436 nm, which is only $\approx 3.5\%$ less than one would predict for cGaN using known values for tetrahedral radii. The growth apparatus and procedures, substrate deposition and surface preparation, as well as the results of chemical and structural analyses of the cGaN films are described in detail in Ref [20].

The in-situ chemical analysis reported below was conducted using X-ray photoelectron spectroscopy (XPS) situated in an UHV chamber connected to the MBE system. X-ray diffractometry, and photo- (PL) and cathodoluminescence (CL) were performed ex-situ. A Philips x-ray diffractometer was utilized for diffraction measurements. Silicon and SiC peaks were used for the calibration of the angular positions of the GaN peaks. Photoluminescence was performed with an Ar⁺ laser (Spectra Physics 2035) tuned to ≈ 300 nm. Emission from cathodoluminescence was achieved by 5 keV excitation.

C. Experimental Results

The in-situ XPS results did not reveal carbon or oxygen contamination within the resolution of the instrument (typically 0.1%), as shown in Figure 7. This is in contrast to the results reported for the chemical analyses of our initial GaN thin films, thus the contamination observed previously [20] originated mainly from the exposure of the films to the atmosphere, prior to the analyses.

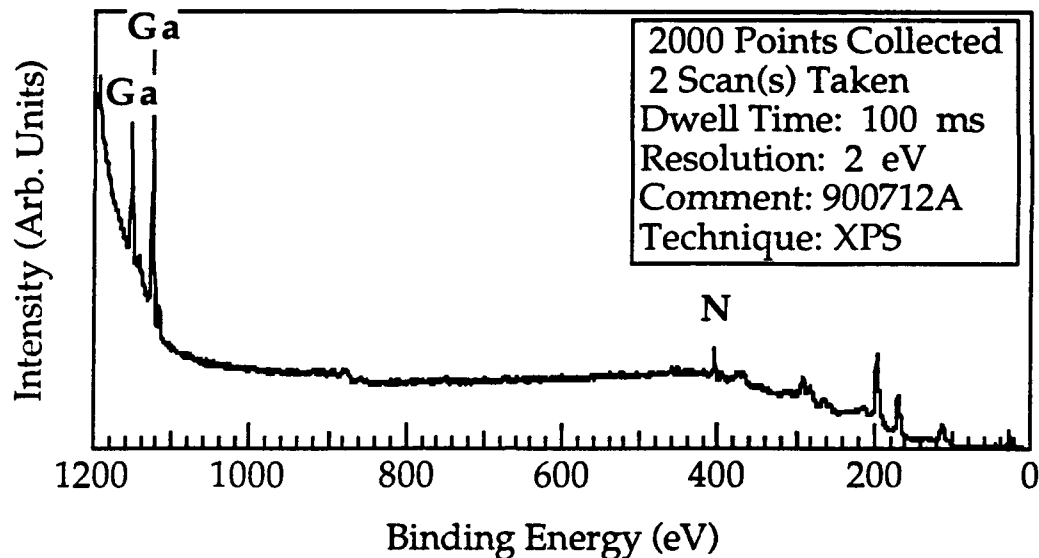


Figure 7. In-situ XPS spectrum of as-grown GaN. Film shows no surface contaminants within the resolution of the technique. The unlabeled low energy peaks are Auger peaks.

From the x-ray data the lattice parameter of cGaN was determined to be 0.451 nm, which is in good agreement with calculated and previously reported values. The resulting x-ray diffraction spectrum is shown in Figure 8. This spectrum also supports the previous analysis [19] regarding the achievement of epitaxial growth, as indicated by the parallel (200) directions of the film and substrate (if they were not, the same low index peaks of the film and substrate would not be observed).

The bandgap determined from the room temperature PL data of wGaN was ≈ 3.44 eV, in agreement with previously reported values. The measured bandgap of the cGaN showed a considerably lower value: 3.28 eV at room temperature and 3.31 eV at 80K. Photoluminescence revealed a broad featureless peak. The full width at half maximum (FWHM) was 30 nm or 0.13 eV. The high peak width is believed to be caused by the strain due to defects piled up at the heteroepitaxial interface (i.e., dislocations, twin boundaries) [27]. Thus GaN does act similarly to SiC in that the bandgap for the cubic phase is more narrow than that for the hexagonal polytype.

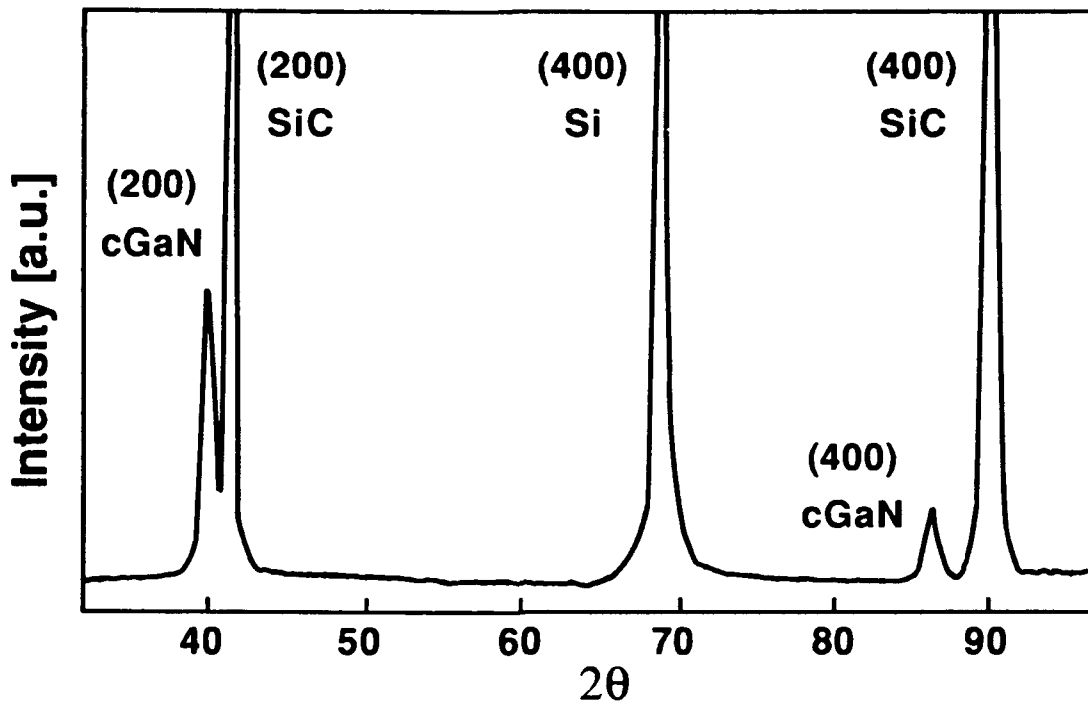


Figure 8. X-ray spectrum of cGaN grown on (100) β -SiC on Si. Silicon (200) and SiC (200) lines were used for calibration. The lattice parameter of cGaN was determined from these results to be 0.451 nm.

The cathodoluminescence (CL) of a cGaN epilayer at 15K showed a cluster of peaks with a high energy shoulder at ≈ 3.33 eV, as shown in Figure 9. A perusal of that cluster shows that it consists of five peaks. The four low energy ones are energetically equally spaced. Their spacing was measured, assuming a Gaussian shape for each of them, to be ≈ 50 meV; their FWHMs ≈ 45 meV. It is believed that the equal spacing arises from phonon interactions and, as such, the low energy side of the observed cluster consists of a zero phonon peak centered at 3.29 eV and three phonon replicas. The exact nature of the high energy peaks located at 3.33 and 3.29 eV is not known, however, it is believed that they originate due to band-to-band and impurity-to-band transitions, respectively.

The energy of the observed phonons is about 20% lower than the TO phonon energies in wGaN and only half of the values measured for LO phonons [28]. Since data on phonons in cGaN do not exist, a direct comparison could not be made. A concise study of Raman scattering in cGaN should be conducted.

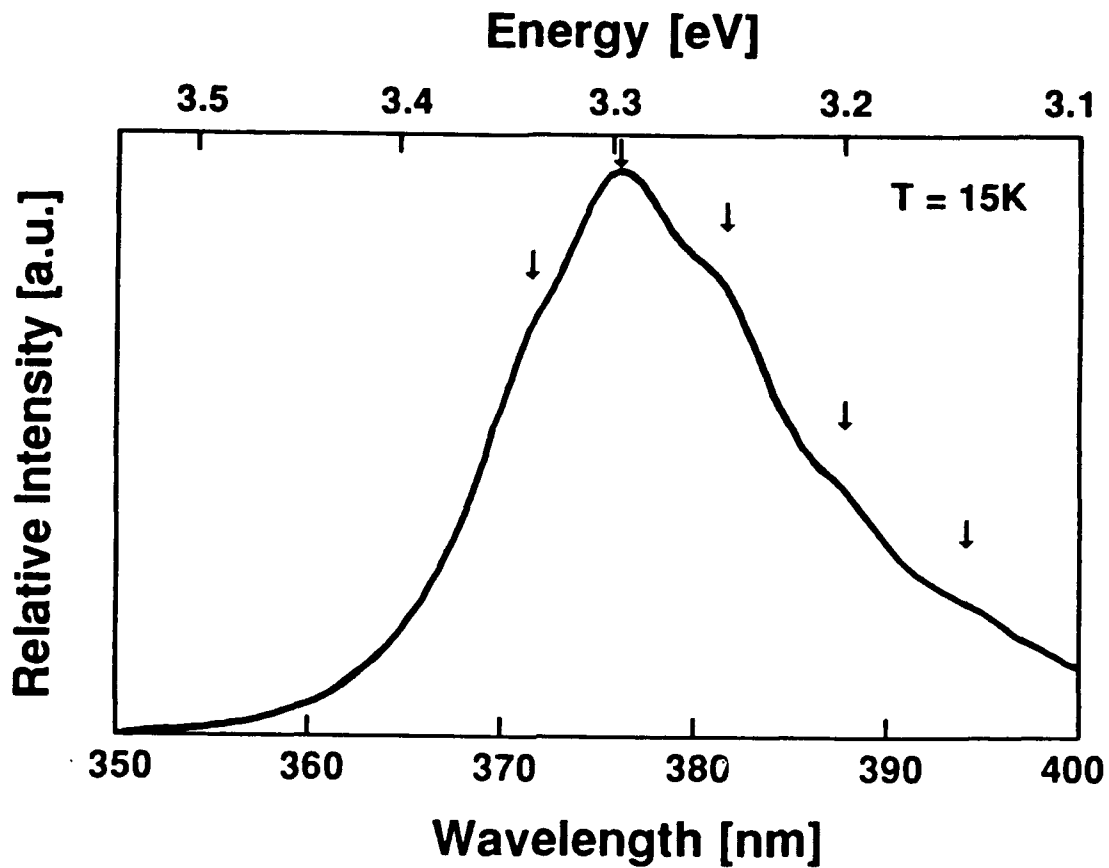


Figure 9. The edge emission of the cathodoluminescence at 15K from a cGaN epitaxial film. The cluster consists of five, in energy equally-spaced peaks. The spacing is ≈ 50 meV, and the arrows denote their positions.

D. Summary

The first photo- and cathodoluminescence results obtained from single crystals of the cubic phase GaN have been reported. The bandgap of cGaN was determined to be 3.33 eV at 15K and 3.28 eV at room temperature, which is 140 and 160 meV lower than respective values for the wurtzite phase. The edge emission of cathodoluminescence at 15K showed a cluster of five equally-spaced peaks. This is believed to be caused by phonons with an energy of ≈ 50 meV. The lattice parameter of 0.451 nm was measured by X-ray diffractometry.

III. The Effect of Electron Beam Irradiation on Mg Doped GaN Thin Films

A. Introduction

Numerous groups have deposited GaN epitaxial thin films [29,30]. However a particular challenge has been the production of p-type material which would allow p-n junctions and GaN-based optoelectronic devices to become a reality. The only devices made to date in this normally n-type material have been metal-insulator-semiconductor (m-i-s) structures, with heavily compensated GaN "i" layer containing up to 10^{22} cm⁻³ of the acceptor dopants of Zn or Mg.

Recently Amano et al. [31,32] observed a dramatic increase of the intensity of the emitted light with time while performing cathodoluminescence measurements on Mg-doped GaN films. Subsequently they found that the resistivity had also increased. Moreover, with sufficiently long electron beam irradiation, the material became p-type and the resistivity decreased. Their films were grown by an organometallic route at 1040°C. The same authors observed similar behavior in Zn-doped GaN thin films [33]. Structural properties remained unchanged after the treatment as was confirmed by x-ray diffraction. However, the mechanisms involved are not yet understood.

The following sections describe the results of similar experiments conducted at NCSU.

B. Experimental Procedure

Magnesium-doped GaN films were deposited on monocrystalline (0001) alpha(6H)-SiC wafers using a modified gas source molecular beam epitaxy (MBE) technique. Effusion cells were used for the evaporation of metallic gallium and magnesium, but a unique, MBE compatible, ECR plasma source [34] was used to activate/dissociate molecular nitrogen prior to deposition. The deposition system as well as the predeposition treatment of the substrates have been described previously [35].

Magnesium-doped GaN films having a thickness $\leq 0.5 \mu\text{m}$ were deposited in the range of 600-700°C on bare or undoped GaN-coated a-SiC wafers. The undoped layers were about 0.3 μm thick. The doping levels were determined by secondary ion mass spectrometry (SIMS) using a Mg implanted GaN reference standard. The implantation energy and the dose for the standard were 50 keV and $3 \times 10^{15} \text{ cm}^{-2}$, respectively.

Two different arrangements were used for the post-growth electron beam irradiation of the films: 1) a 10 kV RHEED gun, placed in one of the ports normally used for an effusion cell on the MBE, and 2) a scanning electron microscope (SEM). The same electron beam energy of 10 keV, was employed; however, the spot sizes, raster areas and the irradiation times were different from that used with the RHEED gun. Table IV shows the parameters for both cases.

Table IV. The parameters of the electron guns used for the post-growth irradiation.

| Electron gun | RHEED | SEM |
|--|-------------------|-------------------|
| Electron energy [keV] | 10 | 10 |
| Spot size [dia- μm] | 1000 | 0.2 |
| Electron current [mA] | 200 | 2 |
| Electron current density [mA/cm ²] | 2.5×10^4 | 1.6×10^9 |
| Raster size [cm ²] | 4 | 1 |
| Irradiation time [hrs] | 4-15 | 1-6 |

Current-voltage (I-V) measurements were conducted before and after selected periods of irradiation using a mercury electrical probe. The diameters of the ohmic and rectifying contacts were five and one mm, respectively. Thermal probe measurements were also performed.

C. Results and Discussion

The low temperature growth produced chemically abrupt junctions between the doped and undoped regions of GaN at all temperatures. Figure 10 shows a SIMS depth profile of a 0.6 μm thick GaN film grown at 600°C. The top 0.45 μm of the film is Mg-doped. Clearly, the diffusion of Mg into the undoped GaN was insignificant during deposition. The Mg atomic concentration levels in the several doped layers were in the range of 10^{20} - 10^{21} cm^{-3} .

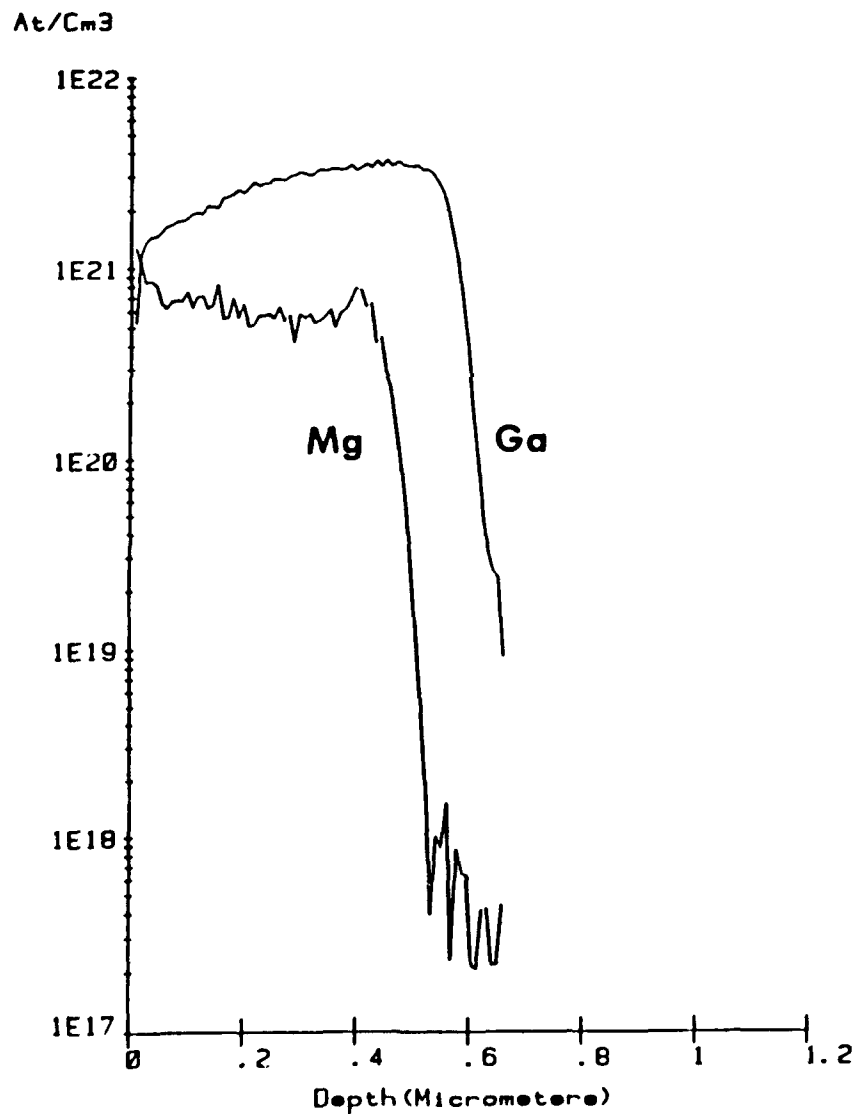


Figure 10. SIMS depth profile of an GaN p-n junction. Mg concentration in the p layer is $\approx 6 \times 10^{21}$ cm^{-3} . Note: concentration scale is for Mg only.

The resistivity of the doped samples increased significantly (a few orders of magnitude) after electron beam irradiation in the SEM. Several samples became p-type, as confirmed by the I-V and thermal probe measurements. Figure 11 shows the change in the I-V curves obtained from a Mg-doped sample after four consecutive one hour LEEBI treatments. Resistivity clearly increased with the irradiation time, and the process appeared to be additive. The curve asymmetry also changed the exposure time. The n-type material is expected to exhibit a larger absolute current with positive

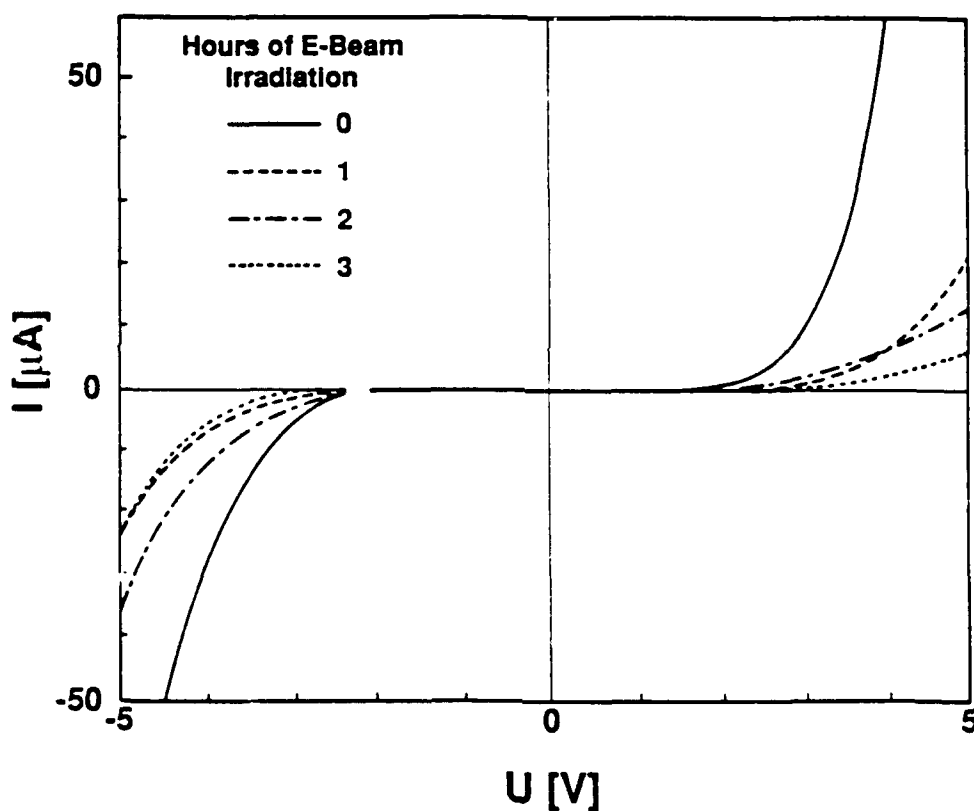


Figure 11: I-V curves of a Mg-doped GaN film before and after three consecutive one hour electron beam irradiations.

than with the same magnitude of negative bias. The opposite is true for p-type material. An apparent change in the symmetry of the I-V curve was observed for a $0.65 \mu\text{m}$ thick sample with a Mg concentration of $8 \times 10^{20} \text{ cm}^{-3}$. The I-V curve is shown in Figure 12. The irradiation time was three hours.

A similar procedure performed in the growth chamber using the RHEED electron gun did not produce any significant changes in the electrical properties of the Mg-doped material even after 15 hrs of irradiation. Although the electron energy from the RHEED gun was similar to that used in the SEM, the spot diameter and electron beam current were different. This difference resulted in almost five orders of magnitude lower electron current density. Thus the electron current density is an important factor in the activation process of dopants via LEEBI in GaN. It has no effect unless a threshold current density has been achieved.

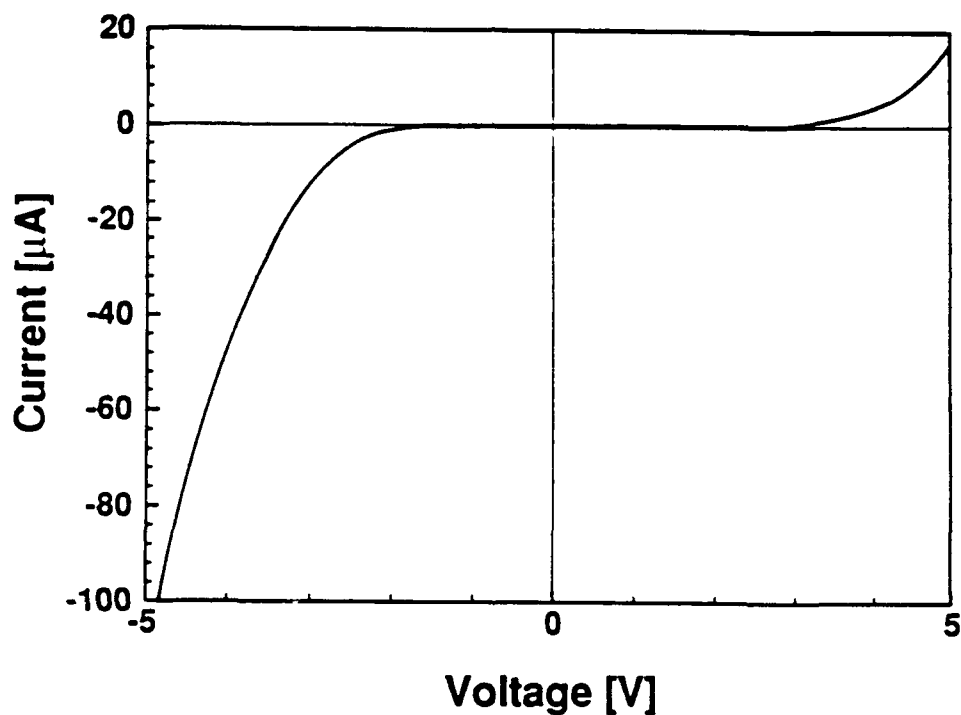


Figure 12. I-V curve of a Mg-doped and LEEBI treated GaN thin film. The irradiation time and Mg concentration were three hours and $8 \times 10^{20} \text{ cm}^{-3}$, respectively.

Several Mg-doped GaN samples clearly showed p-type conductivity, as confirmed by I-V and thermal probe measurements. However, a clear dependence of electrical properties on the irradiation dose was not observed. Moreover, separate

irradiation procedures on the different parts of the same wafer did not yield the same changes in the electrical properties. One of the reasons for this inconsistency (maybe the only one) was probably the poor stability of the electron gun used for the irradiation.

Although Amano et al.³ observed no change in resistivity after the LEEBI treatment of undoped GaN, the resistivity of our undoped samples slightly increased. However the effect was much smaller than with the doped samples.

D. Summary

Monocrystalline Mg-doped GaN thin films have been grown on alpha(6H)-SiC substrates at 600-700°C using modified gas source MBE. SIMS results showed chemically abrupt junctions at all growth temperatures. Samples were post-growth LEEBI treated using a SEM or a RHEED electron gun. Significant changes in the electrical properties including p-type conductivity were observed when the SEM was used, but no changes were obtained with the RHEED gun. The reason for this is most likely the difference in the electron current densities of the two techniques.

IV. Atomic Layer Epitaxy of GaN and AlN

A. Introduction

Atomic layer epitaxy (ALE) is a technique for growing films of materials one atomic layer at a time through a series of self terminating steps. This technique offers monolayer control over film thickness, a low thermal budget, and excellent control over stoichiometry.

The ALE growth of GaN and AlN will be conducted in a newly constructed ultra-high vacuum system specially designed for this purpose. All necessary hardware for handling the selected organometallics has been acquired and is currently being assembled.

GaN and AlN will be grown using TEG (Triethylgallium) and TEA (Triethylaluminum) as metal sources and ammonia as the nitrogen source. TEG and TEA have been chosen instead of TMG and TMA, due to the weaker bond of the ethyl group to the metals. This will allow lower growth temperatures and less carbon incorporation in the films.

B. The ALE System

To accomplish the ALE of GaN and AlN, a vacuum system has been designed and built. A composite drawing of the system is shown in Figure 13. The system is configured to process one inch wafers. Ultimately, the apparatus may be adapted to handle samples up to two inches in diameter. The ultra high vacuum system consists of three modules; a load lock, a cleaning chamber, and a growth chamber. Process gasses will be regulated by thermal mass flow controllers. Hydrogen will be used as a carrier gas for the organometallic sources, TEG and TEA, which will provide gallium and aluminum, while NH₃ will serve as the nitrogen source. Process pumping will be handled by a rotary vane pump, and high vacuum will be achieved through diffusion pumps.

The load lock is a simple five way cross that can hold up to four samples. All samples are introduced to and removed from the system through this chamber. By the present design, the load lock may be pumped to the millitorr level.

After passing through the load lock, the samples are cleaned in the cleaning chamber by a remote hydrogen plasma. The cleaning chamber is pumped by a diffusion pump to high vacuum, and process gas is handled by a rotary vane pump through a throttle valve. To assure identical sample cleaning within a run, up to four samples can be cleaned at a time. This chamber is capable of performing many variations on the plasma cleaning operation, since it has the capability of varying flow rates, substrate temperatures, plasma power, and process pressure.

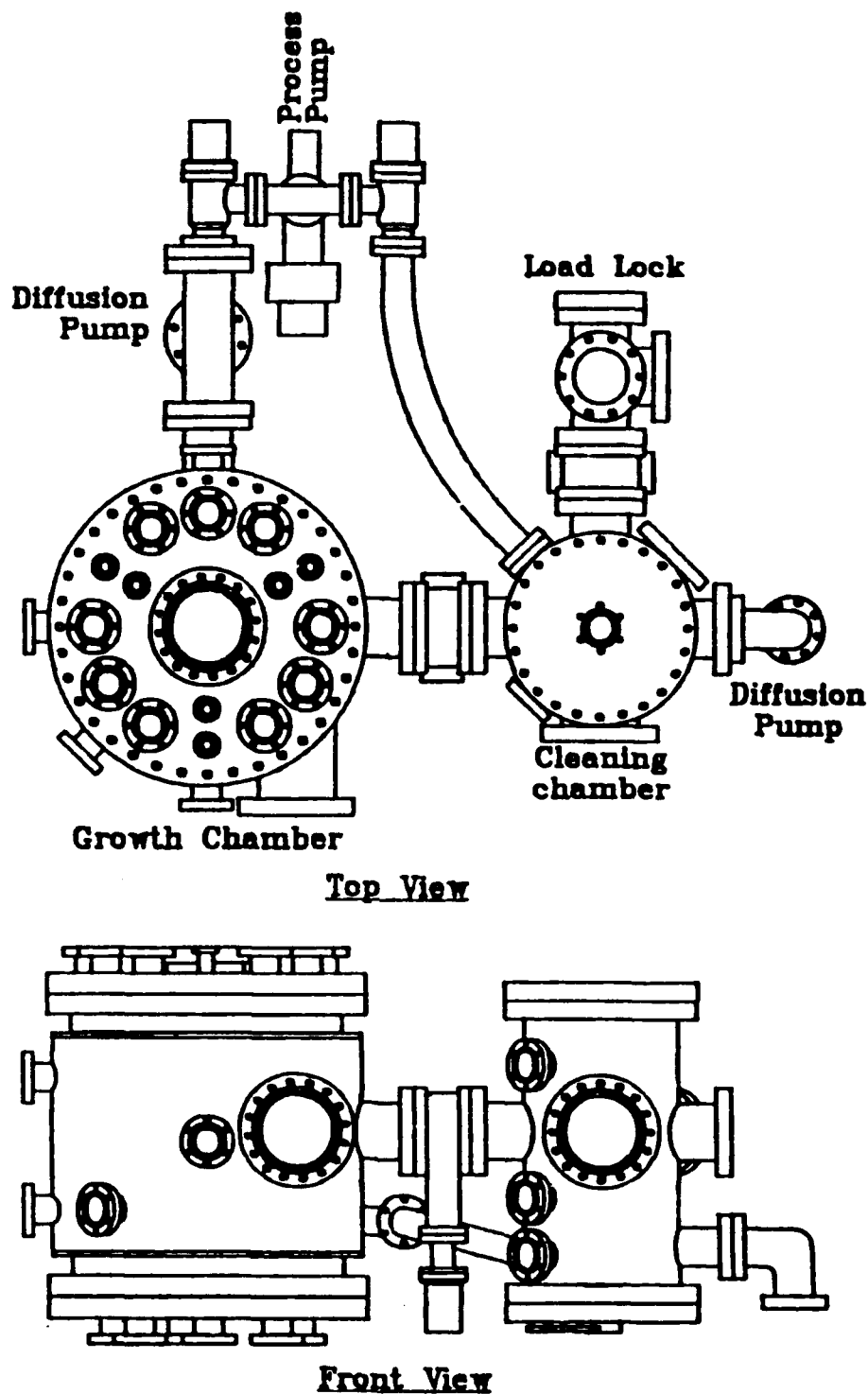


Figure 13: Atomic layer epitaxy system. The top view shows all three chambers: load lock, cleaning chamber and growth chamber, while the growth chamber (left) and the cleaning chamber (right) are visible in the front view.

After cleaning, the samples are transferred to the growth chamber. Like the cleaning chamber, the growth chamber is pumped to high vacuum using a diffusion pump, and process gas is handled by a rotary vane pump through a throttle valve.

Inside the growth chamber, the samples seat on a revolving, heated stage. The heater design allows heating to 1000°C; however, the intention is to process at substantially lower temperatures. Due to the large mass that is heated inside the growth chamber, and the potential high temperatures, appropriate heat shielding, and water cooling have been applied.

The vane assembly, which is stationary above the rotating heating stage has 16 separate compartments for the introduction (theoretically) of up to 16 different gases without mixing. However, the ALE process requires a purge cycle with an inert gas after each exposure of the wafers to the source gas. This allows sufficient time for the desorption of the physisorbed molecules. After this cycle only the chemisorbed monolayer remains. For the growth of GaN and AlN, eight compartments will be used for the purge gas and eight for the source gases: four for TEG or TEA and four for ammonia. This arrangement will allow the growth of four monolayers (about 7-8 Å) of the binary compound per revolution. The anticipated growth rate is about 1 μm per hour. Figure 14 shows the hearth of the ALE system: heater, sample receiver and the vane assembly.

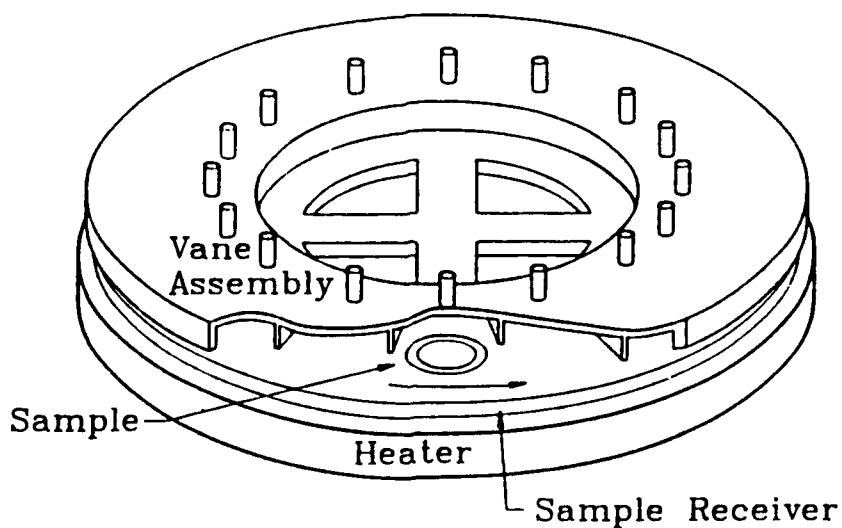


Figure 14: ALE growth system sample heater and vane assembly. The vane assembly consists of 16 separate compartments for the introduction of various gases without mixing.

V. Future Research in GaN and AlN

The research on AlN, GaN thin films and their layered structures in the MBE system will be continued. The main goals are the improvement of the quality of these materials and the growth of p-type GaN and AlN. Mg will be used as the dopant for both compounds. Having achieved the quality and desired electrical properties, all efforts will be focused toward the growth of structures for simple optoelectronic devices.

The final preparations for the ALE growth of GaN, AlN and layered structures of both materials will be conducted simultaneously. The first ALE material is anticipated within a month. Initial growth efforts will be directed toward the establishment of the best growth parameters and the characterization of the grown material. The focus will be subsequently shifted to optoelectronic applications.

A cathodo- and photoluminescence system will be designed and built in order to provide answers regarding the bandgaps and band energy shifts of compounds and superlattices produced from AlN and GaN. The system will be capable of measuring photon energies up to 7 eV.

VI. Growth of Boron Nitride Films via Gas-Source MBE

A. Introduction

Boron nitride has long been known for its desirable properties as a highly insulating as well as a chemically and thermally stable material. It is structurally similar to carbon in that it exists in hexagonal, wurtzitic, and cubic forms. The cubic form has received much interest recently as a possible substrate for the deposition of diamond, due to the similar lattice parameters ($\Delta a_0=1.34\%$) and its wider bandgap [36]. Several approaches have been employed, in the attempt to grow thin films of cubic boron nitride (c-BN). These include reactive diode and rf sputtering, ion implantation, plasma CVD, and ion beam techniques. All these attempts were successful in producing polycrystalline films of c-BN, though predominantly of a mixed

nature with both cubic and other phases present. It appears that most researchers succeeded in the deposition of c-BN if the technique included the input of additional energy from energetic ions during the deposition process. In the present study, growth of cubic boron nitride (zincblende structure) films has been attempted on a variety of substrates and under widely varying conditions. The details of this research are described below.

B. Boron Nitride on Silicon Carbide

1. Overview

Initial attempts to grow c-BN expanded on the previous approaches by attempting to produce an as-grown, lattice matched, epitaxial c-BN material. The overall experimental objective was the growth of single crystal, cubic gallium nitride [37] ($a_0=4.508 \text{ \AA}$) films on β -SiC (100) films followed by the growth of a graded composition layer from c-GaN to c-BN and finally a layer of c-BN. If complete solubility exists between c-GaN and c-BN, the final composition should have a lattice parameter sufficiently close to c-BN to produce single crystal thin films of the latter material. In addition, the use of a microwave electron cyclotron resonance (ECR) plasma source provided ion bombardment for formation of the cubic phase.

Growth studies were conducted on in-house produced (100)-oriented cubic β -SiC substrates. A detailed description of the substrate preparation is reported in Reference 38. The range of conditions used during growth are given in Table V.

TABLE V. Conditions used in GaN-BN growth

| | |
|--------------------------|--|
| Nitrogen pressure | $5 \times 10^{-5} - 1 \times 10^{-4}$ Torr |
| Microwave power | 50 W |
| Gallium temperature | 850 - 990°C |
| Boron temperature | 1500 - 1750°C |
| Substrate temperature | 600 - 700°C |
| Growth time (BN) | 120 - 360 min. |
| Deposited film thickness | 10-850 \AA (BN) |

2. Chemical Analysis

Scanning Auger analysis (JEOL JAMP-30) was performed on each sample to determine the presence of impurities and the nominal composition of the BN layer. Figure 15 is an Auger spectrum taken from the untreated growth surface. The oxygen peak is due to surface oxidation upon exposure to the atmosphere. The carbon peak is often observed to be surface contamination, but is significant in this case as will be described below. No other contaminants were observed within the resolution of the instrument (typically ≈ 0.2 at.%).

A depth profile was subsequently obtained and is shown in Figure 16. The BN layer thickness is estimated (from SiO_2 sputter rate) to be $\approx 850 \text{ \AA}$, while the BN-GaN mixed layer is $\approx 1000 \text{ \AA}$, and the GaN buffer layer is $\approx 1800 \text{ \AA}$. The oxygen signal remains near the noise level of the instrument throughout the film and thus is not present in significant concentrations.

The depth profile shows that the carbon contamination was significant, and generally followed the boron concentration. After correcting for elemental sensitivities, the B/N ratio is ≈ 1 , despite the high levels of carbon present throughout the layer. The specific source of the carbon contamination is not understood at present, since a number of carbon-free films were grown after a carbon crucible was replaced by one made of pyrolytic BN.

Diagnosis of the source of carbon contamination in the BN films was carried out as follows. A series of samples were grown under a number of different operating conditions and subsequently analyzed by Auger microscopy to identify the conditions that maximized the carbon concentration. It appears now that the carbon is not coming from the high temperature boron effusion cell as previously reported [39]. One source of carbon was identified as being in the incoming nitrogen gas supply. This source was originally discounted, since carbon had not been seen in growths of AlN (which is also a carbide former). However, it appears at present, that boron is a

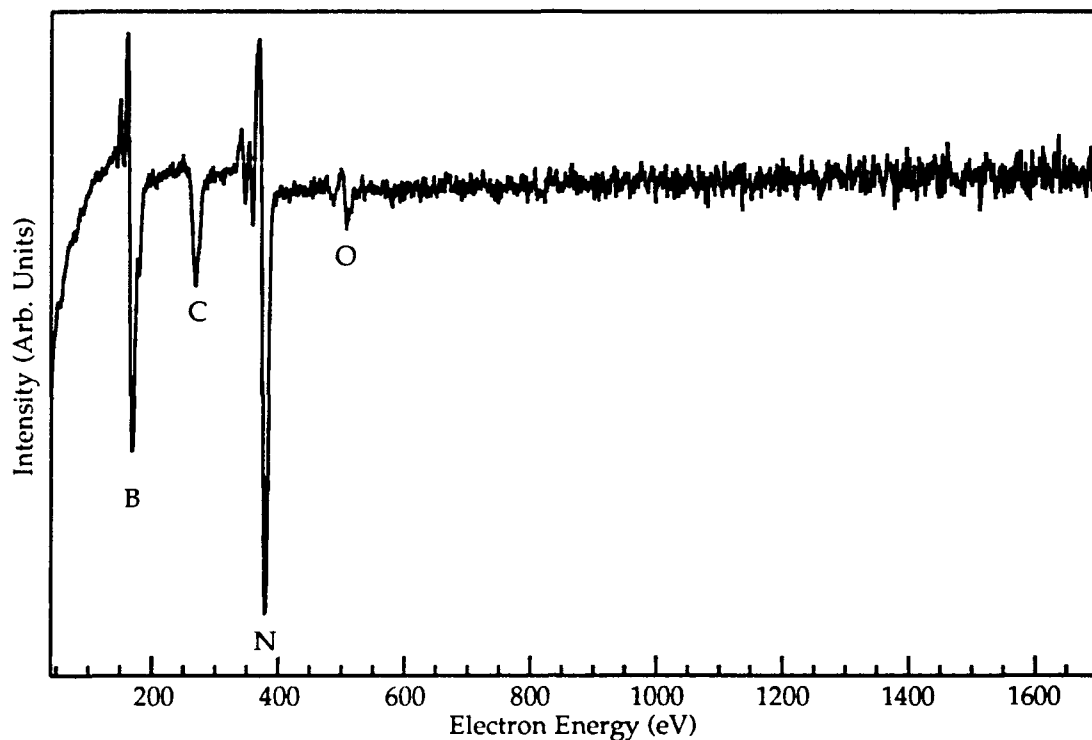


Figure 15. Auger spectra taken from the untreated BN surface. Only oxygen and carbon contamination was detected.

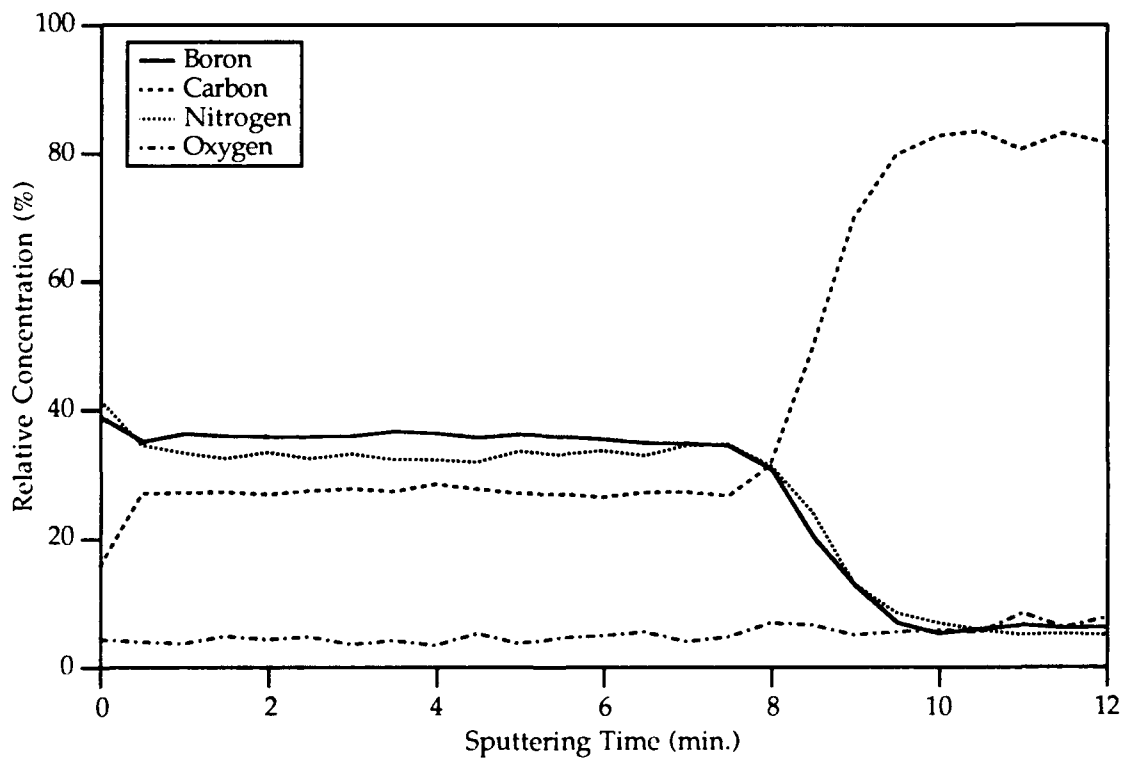


Figure 16. Auger depth profile of the BN layers on β -SiC (100). The profile of the carbon contamination follows that of the boron concentration. The thickness of the BN film is $\approx 850 \text{ \AA}$, and the graded layer is $\approx 1000 \text{ \AA}$.

much stronger carbide former as well as being grown at lower growth rates has contributed to its appearance in the BN films. A second gas purifier was installed to reduce the hydrocarbon contamination in the incoming nitrogen gas to <10 ppb levels. Growths shortly after installation showed improvement in the carbon levels, but not elimination. Nearly complete carbon elimination was achieved after repair of the graphite heater stage assembly on the MBE growth manipulator. The exact nature of this mechanism is unknown since carbon diffusion rates are extremely low at the growth temperatures used. It is speculated that some sort of gas phase transport mechanism was involved. The purity of the as-grown film surfaces after both of these modifications were made can be seen from the XPS spectra in the later section on growth of BN on Si (100).

Given the relative purity of the films now produced, an effort was made to quantify the N/B ratio. To get accurate N/B ratios requires that an independent standard be analyzed by the same analytical system used to evaluate the films. To this end a sample of high purity (99.99% min.) pyrolytic BN (Boralloy™, Union Carbide) was obtained. This sample was analyzed by our XPS system and resulted in a relative N/B sensitivity factor of 3.68, which is very close to the value of 3.70 published by Surface Science Laboratories, Inc.

3. Structural Analysis

Reflection high-energy electron diffraction performed during growth indicated that the B_{0.7}GaN film remained predominantly single crystal, but shows both a normal cubic [110] pattern and a second hexagonal pattern [01 $\bar{1}$ 0]. By contrast, during the deposition of the BN, the RHEED pattern indicated that this film was predominantly amorphous with some microcrystallinity also present.

Transmission electron microscopy (TEM) was used (Hitachi H-800) to more closely examine the microstructural evolution of the BN/B_{0.7}GaN/GaN epitaxial films. Cross-section TEM specimens were prepared using standard techniques described in

Reference 40. Examination in bright-field and with selected area diffraction (SAD) also showed the BGaN layer to be a mixture of cubic and wurtzitic phases. This layer was heavily faulted. The latter phenomenon is to be expected given the high degree of lattice mismatch (19.8%) being accommodated in a layer of only 1000 Å. Examination of the diffraction patterns taken from the BN film revealed this layer to be amorphous, as shown in Figure 17. Only the top film of the multilayer assembly is shown (a-BN), which displays a contrast similar to the epoxy. The BGaN layer is nearly opaque because its lower ion milling rate left it much thicker than the BN layer.

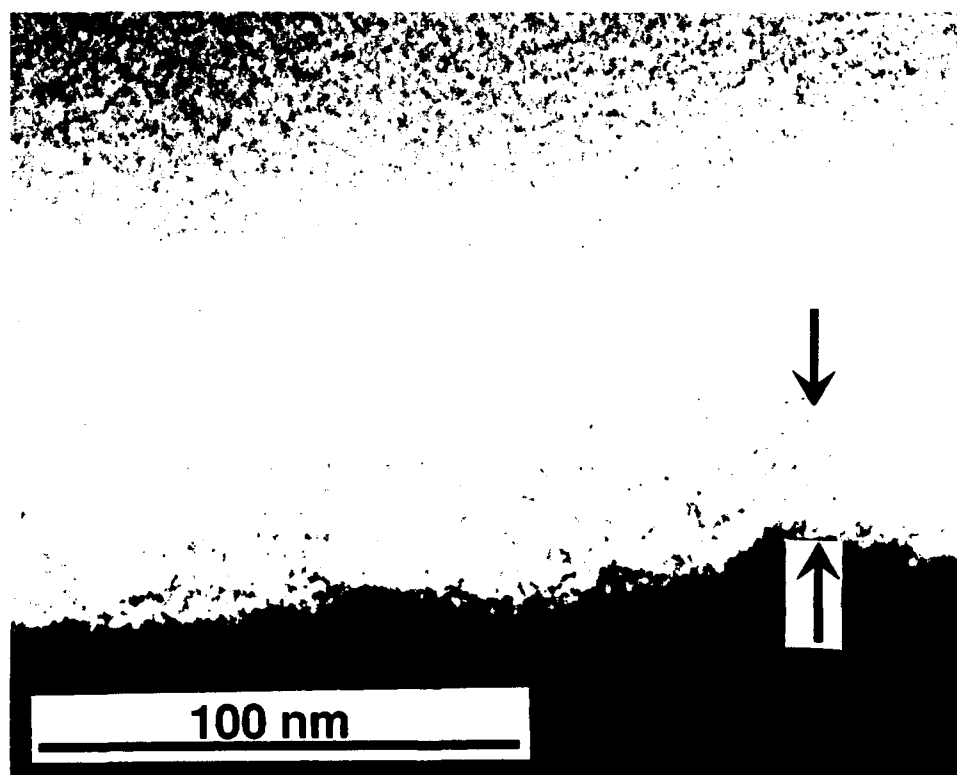


Figure 17. XTEM photograph ($z=[110]$) of the top of the deposited film with the BN marked. The low contrast of the layer is due to its amorphous nature (see text).

Scanning electron microscopy (SEM) examination of the surface of the film was performed to evaluate the surface morphology produced during the deposition. The resulting morphology was quite good as can be seen in Figure 18.

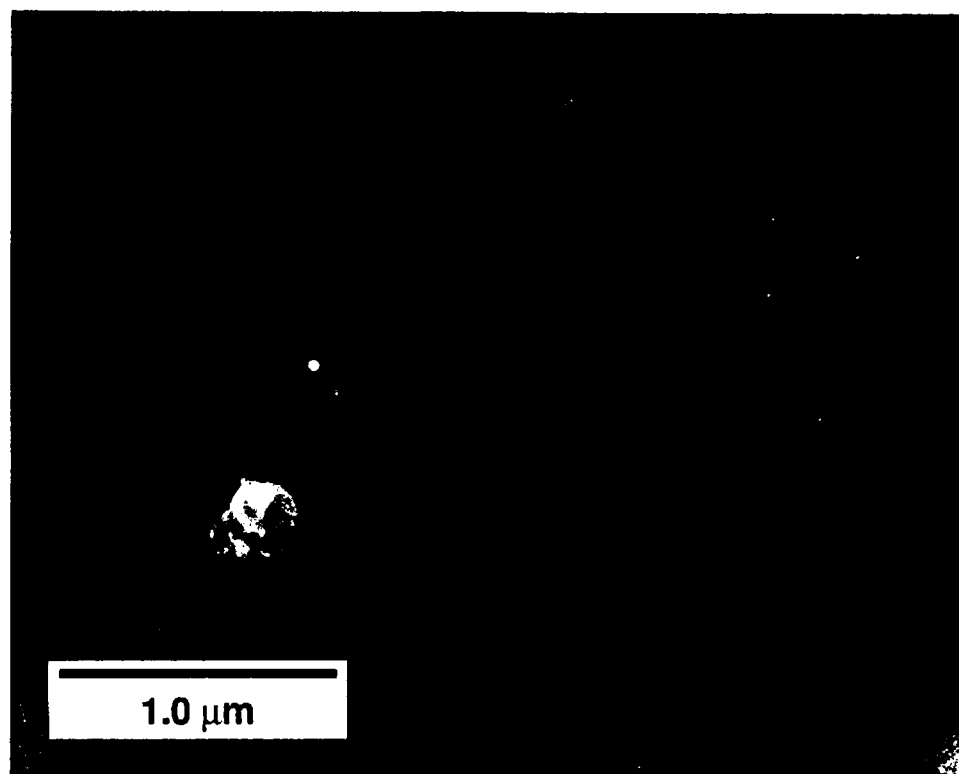


Figure 18. SEM photograph of the surface of the deposited film. The white particles on the surface appear to be contaminants that adhered after the samples exposure to the atmosphere.

C. Boron Nitride on Diamond (100)

Diamond (100) substrates (4 mm × 4 mm × 0.25 mm, type IIa) were purchased from Dubbledee Harris Diamond Corp., in an attempt to grow c-BN (100) layers on it. Diamond makes a nearly ideal substrate for c-BN, due to its low lattice mismatch ($\approx 1.4\%$) and higher surface energy, which both promote two-dimensional growth.

The diamond substrates were degreased in a series of organic solvents (trichloroethylene, acetone, methanol and isopropanol) to remove hydrocarbon residues. Subsequent examination in a field emission SEM (Hitachi S-4000) revealed a rough surface morphology, which is shown in Figure 19.

After these investigations, it became apparent that the polishing procedures might well leave graphitic and/or highly damaged diamond layers on the surface which would in turn interfere with the proper initiation of c-BN growth on its surface. Thus, a

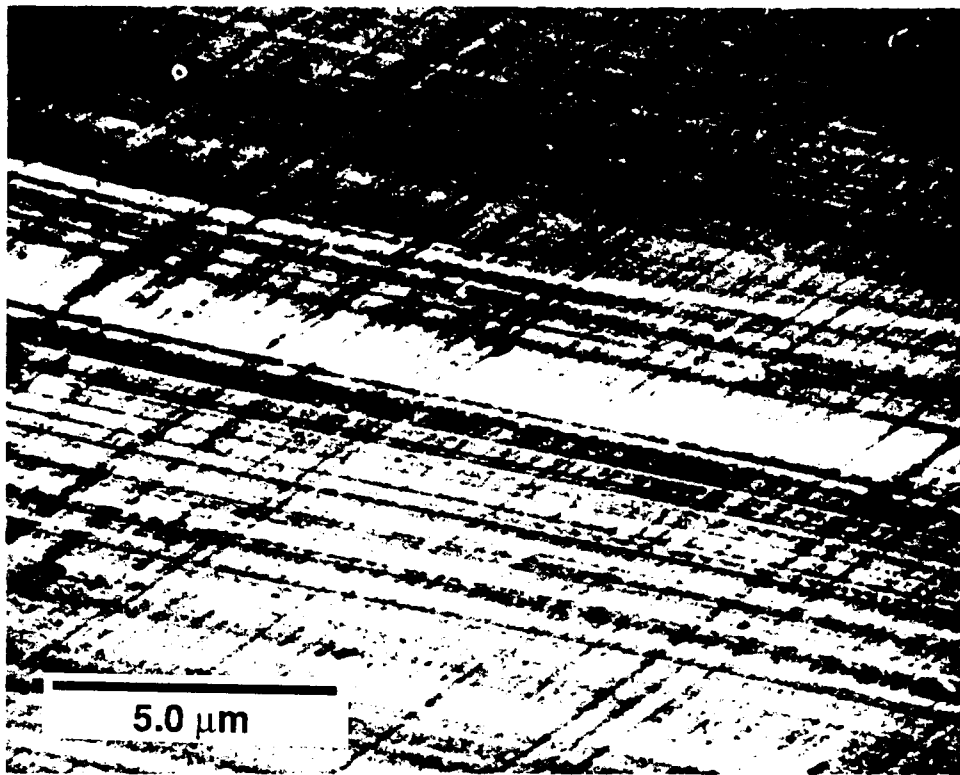


Figure 19. Scanning electron microscope photograph of the unetched but thoroughly degreased diamond surface. Note the appearance of the polishing scratches in conjunction with a dark carbonaceous or hydrocarbon-like deposit.

graphite etching procedure reported in the literature [44] was added to the substrate preparation procedures. This etch involves soaking for 45 min. in a heated solution of $\text{H}_2\text{SO}_4:\text{HNO}_3:\text{HClO}_4$ in the proportions 3:4:1. Figure 20 shows the the surface morphology produced by this procedure.

Note that polishing artifacts are much less pronounced in this micrograph, but a heavily stepped surface was revealed by the etching procedure. It would appear that there was a substantial graphitic or damaged layer present which was removed by the etchant. The highly stepped surface, while not a major obstacle for current growth studies, does pose a serious problem for future research involving device development.

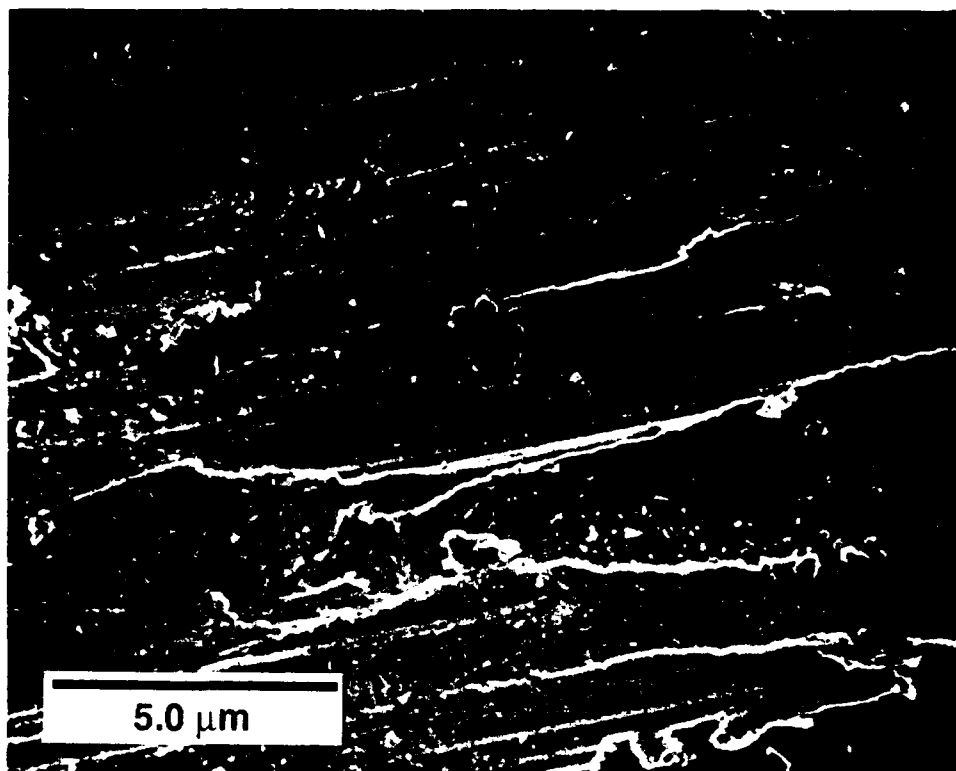


Figure 20. Scanning electron micrograph of the diamond surface after an oxidizing etch to remove graphitic layers.

As a result, discussions were held with representatives of Dubbledee Harris Diamond Corp. and their European supplier regarding these findings resulted in a commitment by them to perform additional quality control tests on the next shipment of diamond substrates. When these new substrates arrive, the same tests will be performed in our laboratories to provide verification of their results. These strenuous evaluation procedures will hopefully result in higher quality diamond substrates for this as well as future studies.

After the cleaning and etching procedures were completed, the diamond samples were rinsed in DI water and dried and then mounted onto a silicon wafer using a commercial ceramic adhesive (Ceramabond™ 503, Aremco Products, Inc.). The silicon wafer was then indium bonded to the molybdenum MBE substrate block. This procedure was used to avoid indium diffusion onto the diamond surface, which readily occurs on 0.25 mm thick α -SiC substrates.

The substrates were then loaded into the MBE system and degassed to 800°C. Higher temperatures for degassing which are typical for silicon processing were not used to avoid graphitizing the surface in the UHV conditions. Typical growth conditions are shown in Table VI.

TABLE VI. Conditions used in growth of BN on diamond

| | |
|------------------------------------|-------------------------|
| Nitrogen pressure | 1×10^{-4} Torr |
| Microwave power | 50 W |
| Boron temperature | 1500 – 1750°C |
| Substrate temperature | 400 – 700°C |
| Growth time | 120 – 480 min. |
| Deposited film thickness (approx.) | 10–1100 Å |

After growth the samples were removed and evaluated using x-ray diffraction. AES was not performed due to the charging of the film/substrate. XPS was also not done due to difficulties with the small sample size, though it would be expected that the composition of the film would not differ from that observed on other substrates. X-ray diffraction indicated that the films were a mixture of graphitic and cubic BN. Interestingly, it appears that the c-BN present was oriented to the substrate, since only the (100) and (200) peaks from the c-BN were observed (see Figure 21), which would not be possible if it were randomly oriented. This is because the c-BN (220) and (111) are stronger reflections, 3X and 50X, respectively, than the observed (200) reflection. Therefore, crystals in these orientations would have been easily observed, even in relatively smaller fractions of the deposited film.

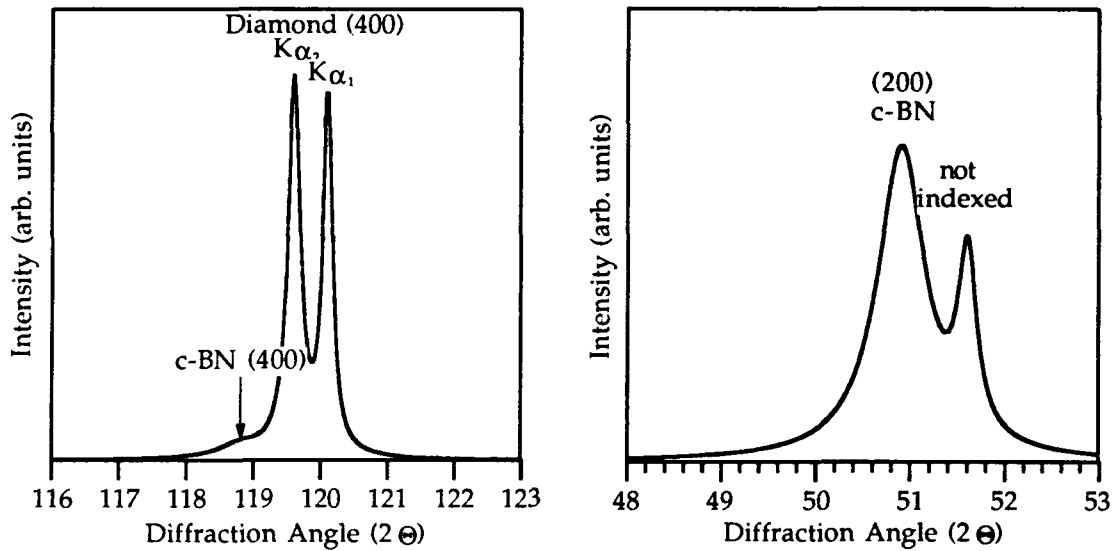


Figure 21. X-ray spectra ($\text{CuK}\alpha$) of BN on diamond. (Left) Diamond and c-BN (400) reflections. (Right) c-BN (200) reflection, since diamond (200) is forbidden by the structure factor.

D. Boron Nitride on Silicon (100)

1. Overview

The orientation observed by Doll *et al* [42] for c-BN on Si was c-BN(100)||Si(100) and c-BN<001>||Si<011>. This orientation presents to the growing c-BN layer a periodicity of $(1/\sqrt{2} \times 1/\sqrt{2})R45^\circ$, which is shown in Figure 22. Note that the new periodic "net" is shown displaced in the figure and located in the next growth sites available above the Si (100) surface.

This new lattice is 6% larger than c-BN, which is much lower than the 33% difference if the lattices are in perfect registry. The appearance of this coincidence condition for c-BN on Si encouraged work on Si as a substrate material.

Another alternative boron source was investigated at the same time the growths began using Si (100) substrates. Borazine ($\text{B}_3\text{N}_3\text{H}_6$) was purchased (Callery Chemical Company) and installed in the gas supply lines for the ECR source in a bubbler configuration. As such, nitrogen was used as a carrier gas which passed through a controlled temperature bath containing the borazine. The controlled

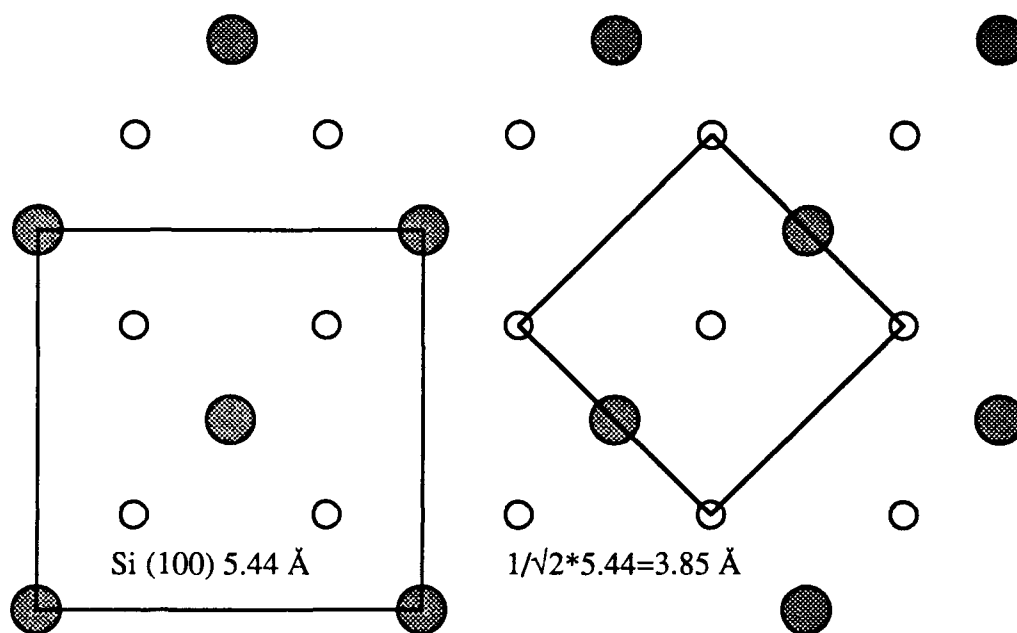


Figure 22. Schematic diagram of Si (100) face, showing the periodicity of $(1/\sqrt{2} \times 1/\sqrt{2})R45^\circ$ possible on this face, displaced upward to the next growth location above the Si surface.

temperature of the bath limited the vapor pressure of the borazine and thus controlled the flow rate of the borazine. This nitrogen/borazine gas was then passed through the ECR source and on to the substrate. Conditions used in the MBE system for deposition both with the borazine and the high temperature boron effusion cell are listed in Table VII.

TABLE VII. Conditions used in BN laser ablation on silicon growth

| | |
|------------------------------------|--------------------|
| Nitrogen pressure | 1×10^{-4} |
| Microwave power | 25 – 50 W |
| Boron temperature | 1700 – 1850°C |
| Borazine bath temperature | -10°C |
| Substrate temperature | 600 – 700°C |
| Growth time | 120 – 480 min. |
| Deposited film thickness (approx.) | 250–1100 Å |

2. Chemical Analysis

Chemical analysis of the resulting films was performed using an XPS system attached to the MBE system allowing in-vacuum transfers and thus analysis of the films without exposure to the atmosphere. Figure 23 shows the spectra obtained for films using the high temperature effusion cell as a boron source. Note the lack of contamination of the films by oxygen and carbon. Use of a standard material permitted calculation of the N/B ratio, which in this case, showed the presence of a nitrogen-rich film. It is unclear at present whether the excess nitrogen plays an important role in the structure of the resulting films.

Figure 24 shows the spectra obtained for films using the borazine bubbler as a boron source. Note the lack of contamination of the films by oxygen and carbon. Use of a standard material permitted calculation of the N/B ratio, which in this case showed the presence of a slightly nitrogen-rich film.

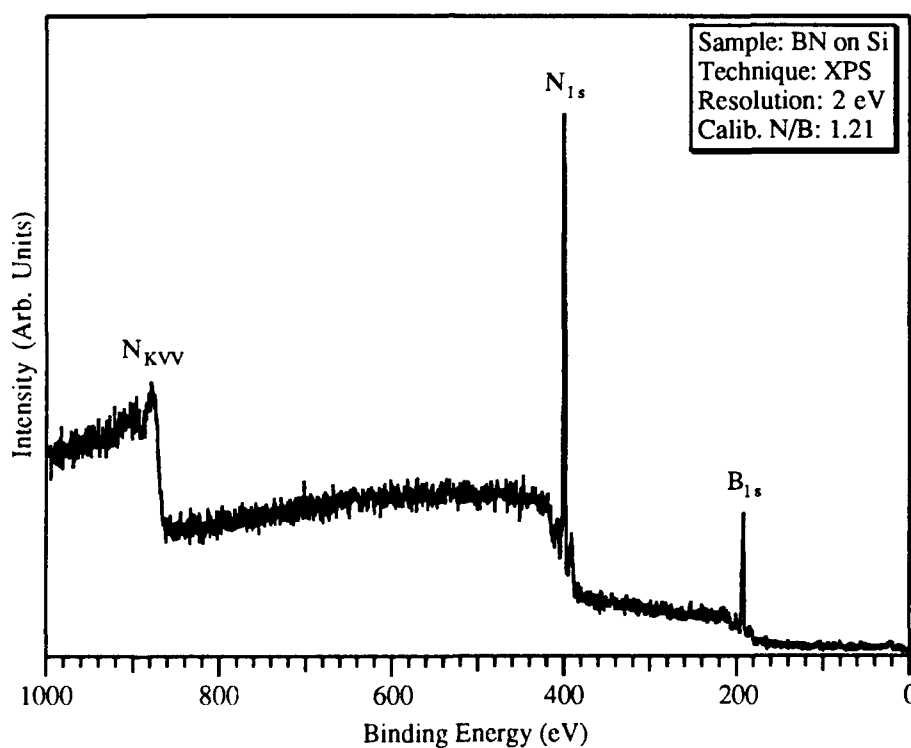


Figure 23. XPS spectra (Mg anode) of BN film grown using high temperature effusion cell as the source of boron. Note the high excess nitrogen present, but no contamination present.

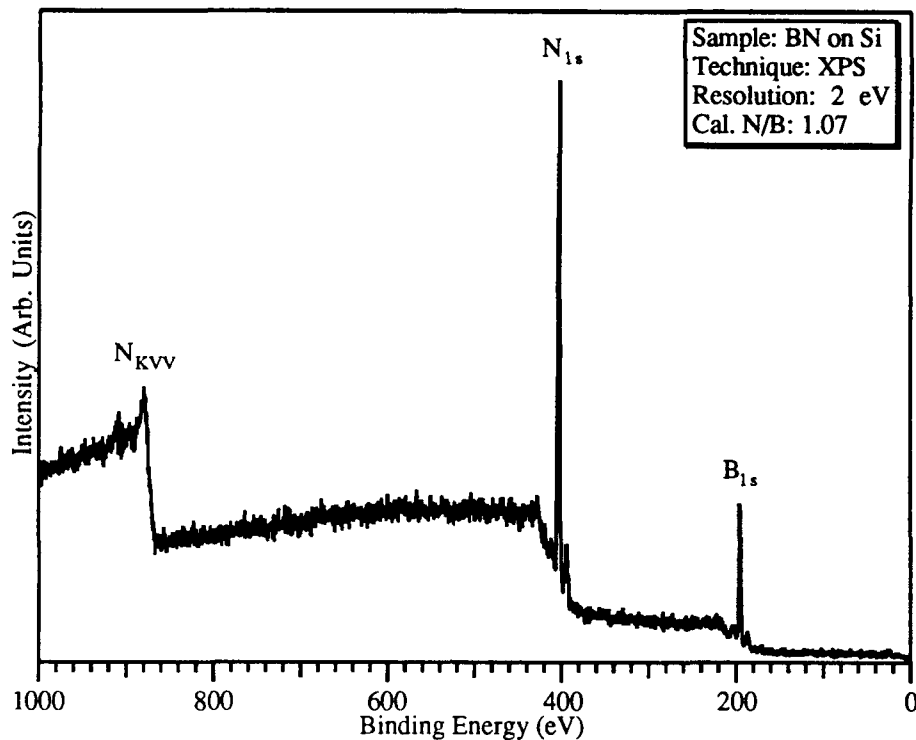


Figure 24. XPS spectra (Mg anode) of BN film grown using borazine as the source of the boron. Note lack of contaminants present.

3. Structural and Microstructural Analyses

Structural analysis of the resulting films began with x-ray diffraction using an automated Rigaku diffractometer utilizing $\text{CuK}\alpha$ radiation. The resulting spectra are shown in Figures 25 and 26. The extremely sharp peaks, which even resolve the $\text{K}\alpha_1$ and $\text{K}\alpha_2$ lines, correspond to the exact position of the c-BN (400) peak. It was initially assumed that since the c-BN (111) peak was not present (and has the highest relative intensity) that the films were highly oriented to the substrate. The sharpness of the peaks could not be explained, however, since extremely thin films even of relatively good quality show appreciable line broadening. As will be shown in the following electron microscopy analysis, the films were shown to be microcrystalline in nature.

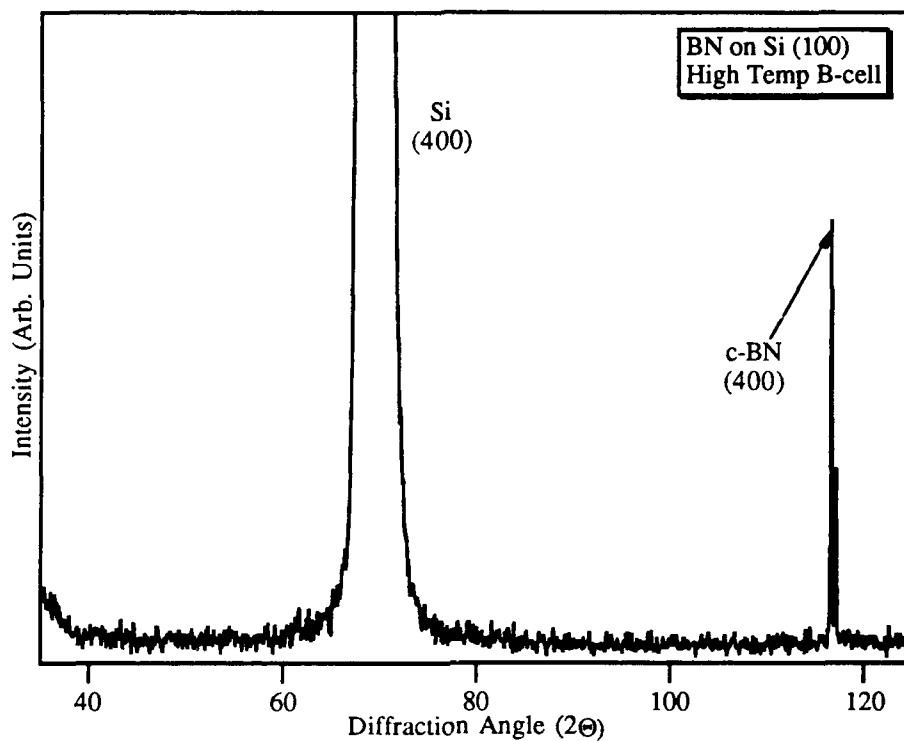


Figure 25. X-ray spectra ($\text{CuK}\alpha$) of BN on Si (100) using high temperature boron effusion cell as a source.

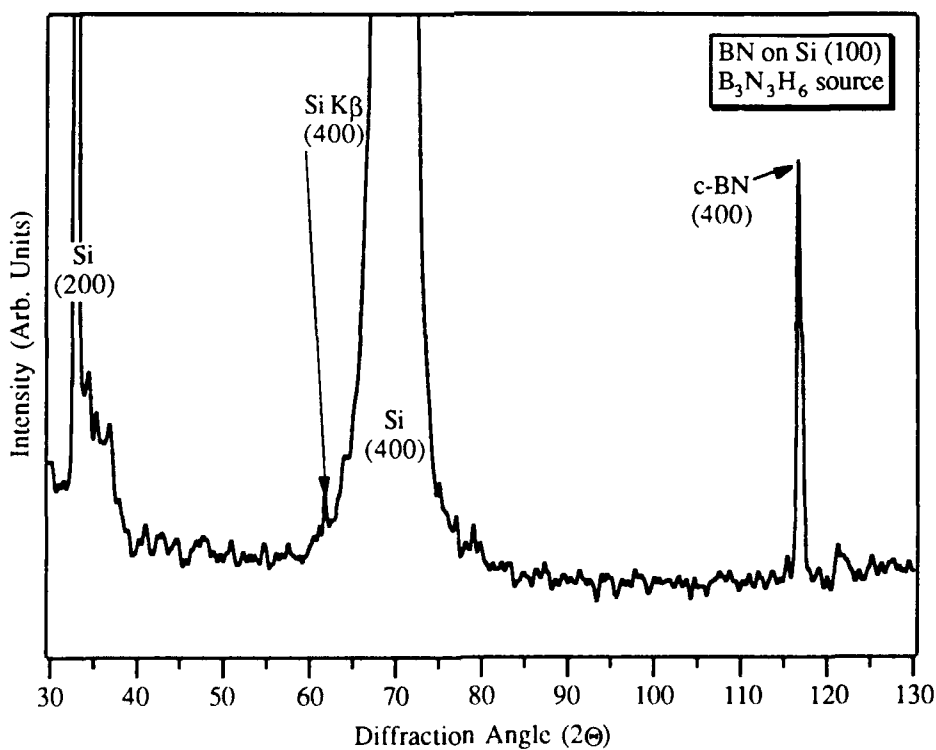


Figure 26. X-ray spectra ($\text{CuK}\alpha$) of BN on Si (100) using borazine as a source.

After x-ray diffraction analysis, backthinned plan-view TEM samples were prepared and analyzed. Figures 27 and 28 show a bright field image and the corresponding SAD pattern of the BN film. Micrographs from both materials are not shown as they are essentially the same. Note the appearance of the fine microcrystals randomly oriented across the film.

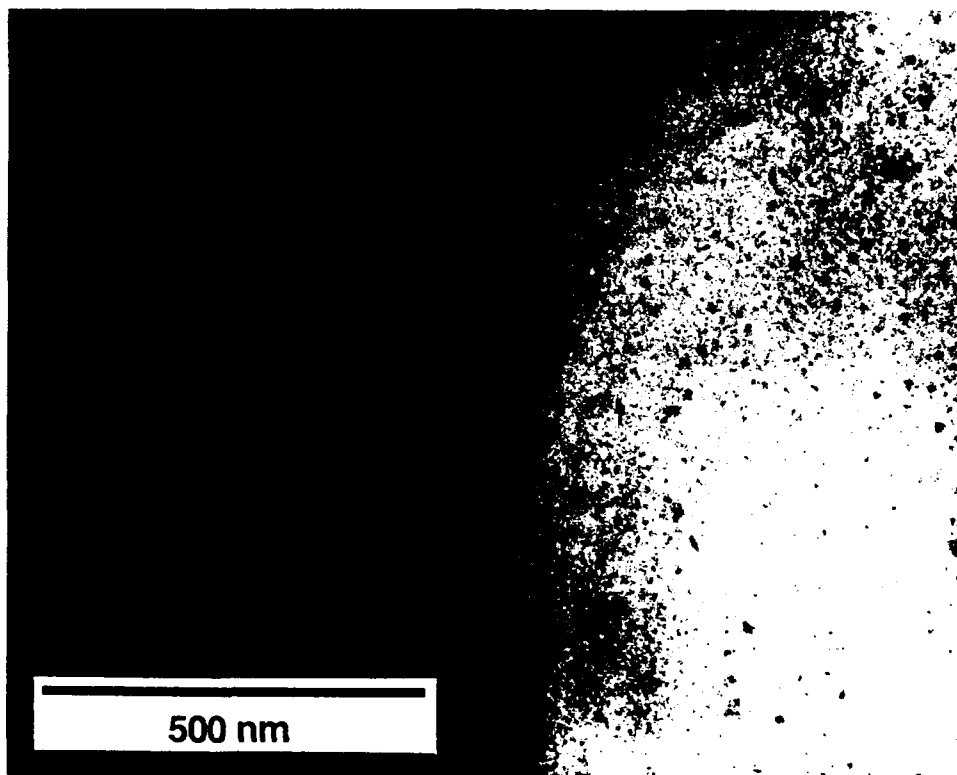


Figure 27. Backthinned plan-view ($z=[100]$) of BN on Si (100). Note evidence of small microcrystals scattered randomly across the surface.

The SAD pattern (Figure 28) shows that the film is random microcrystalline BN as indicated by the broad rings. Additional amorphous character is also observed by the increased diffuse scattering between the rings. The patterns indicate c-BN, but this is not conclusive by itself as h-BN would place rings in nearly the identical locations. However, there is no evidence of the h-BN (002) ring which has the highest relative intensity and is unique to that phase.

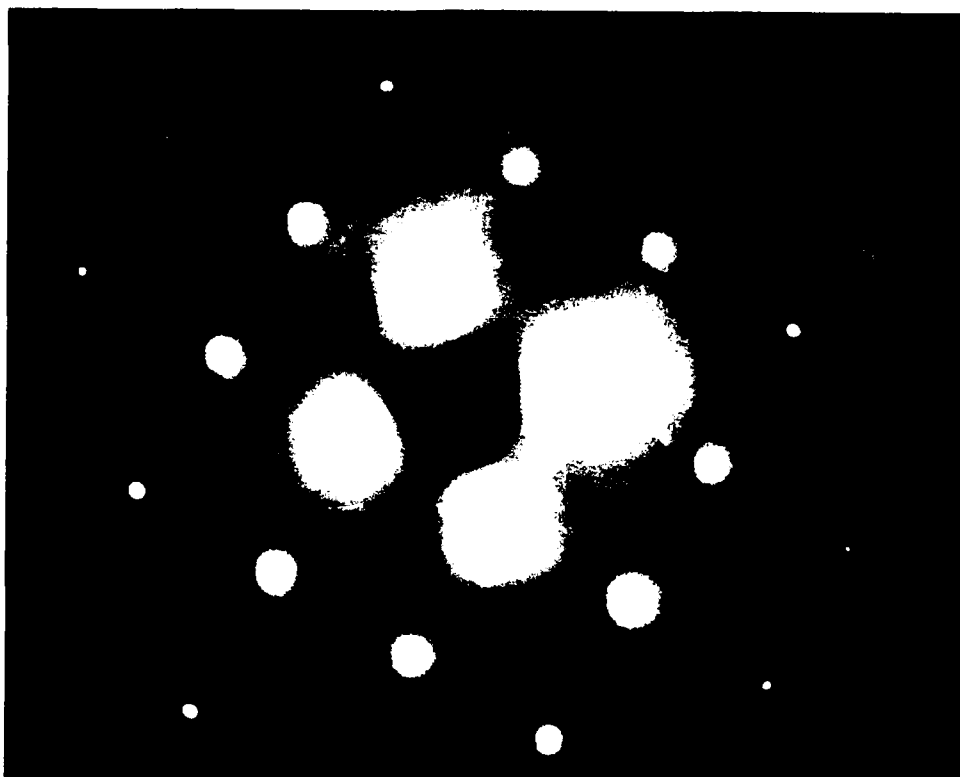


Figure 28. Selected area diffraction pattern ($z=[100]$) of BN on Si (100). Spots are from the Si (100) substrate.

Shown in the Figure 29 is a high resolution SEM photograph of the as-deposited surface of BN on Si (100). Note the textured and pitted nature of the surface, which is otherwise quite smooth and featureless. This texturing is also observed in the case of other nitride growths in this MBE system, and thus may represent an ion bombardment effect, rather than crystalline versus amorphous phases of the BN.

This observed surface compares well the that seen in the plan-view TEM photograph shown in the following figure. Comparison of the feature size in these two figures indicate that these are the same or related features in both.

Additionally, dark field images using the rings and amorphous background indicate that the particles observed are from the deposited film and not the Si substrate.

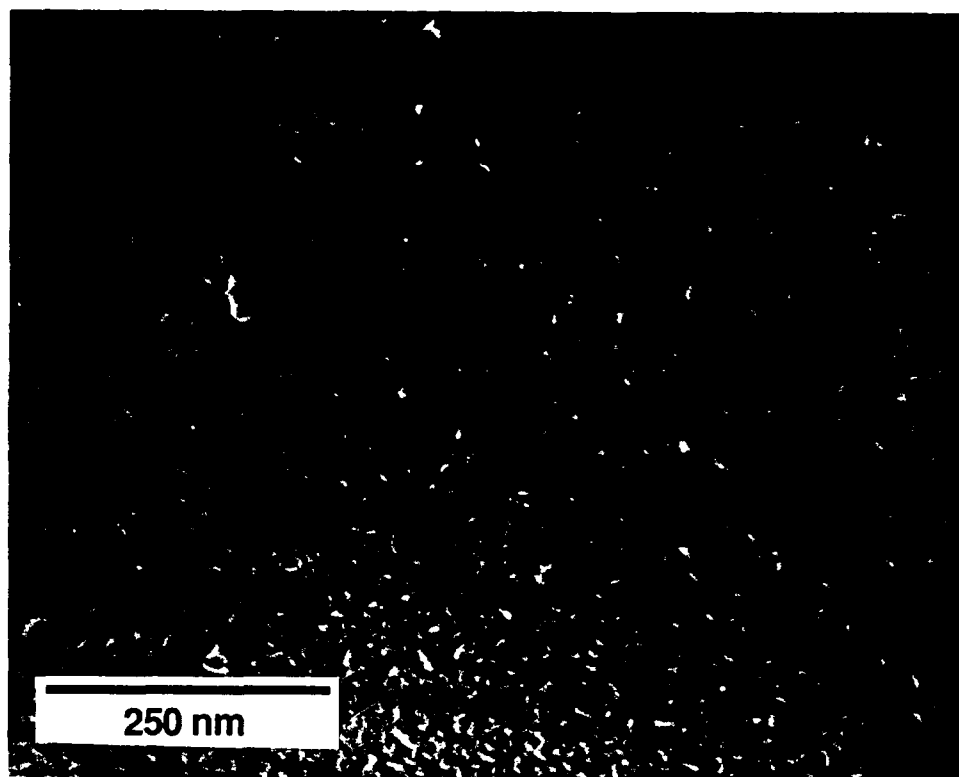


Figure 29. High resolution SEM (Hitachi S-4000) photograph of the as-deposited surface of BN on Si (100). Note fine texturing of substrate surface.

Subsequent to the TEM and SEM analysis, additional samples were prepared for Raman spectroscopy which was performed by Trevor Humphries in the laboratory of Professor Robert Nemanich in the Physics department of NCSU. The resulting spectra were compared to the literature on Raman spectra of BN [43], as well as the Sumitomo c-BN and Union Carbide h-BN and no evidence of the hexagonal peak at 1368 cm^{-1} was observed. However, only slight cubic-like features were observed shifted down from the normal peak locations at 1055 cm^{-1} (TO mode) and 1308 cm^{-1} (LO mode).

In conclusion, the films produced to date on Si (100) substrates are comprised of mainly amorphous BN with some c-BN microcrystallinity, but without hexagonal character.

VII. Growth of Boron Nitride Films via Laser Ablation

Work has begun on laser ablation of BN targets to deposit cubic BN films. This work is being done in collaboration with A. F. Schreiner in Chemistry and O. H. Auciello in Materials Science and Engineering, both of NCSU. The technique involves the use of a pulsed ArF laser ($\lambda=193$ nm) passing through a special UV-grade quartz window into a UHV chamber where it strikes a BN target. The conditions used to date in this study are given in Table VIII. The target ablates under the high energies imparted by the laser pulse and are subsequently deposited on a substrate. A quartz crystal deposition monitor is mounted in the ablation path to permit monitoring of the deposition thickness and rate.

It is thought that the activated material ejected from the surface may provide the necessary energy to allow the depositing BN to crystallize on the substrate in the cubic phase. This is supported by Doll *et al* [42], who deposited c-BN layers on silicon and the fact that polycrystalline TiN has been deposited on a room temperature substrate via laser ablation. The system also has facilities for heating the substrate.

TABLE VIII. Conditions used in BN laser ablation on silicon growth

| | |
|-------------------------------------|--|
| Nitrogen pressure | $1 \times 10^{-4} - 3 \times 10^{-2}$ Torr |
| Average laser power | 0.1–0.55 W |
| Laser pulse | 20 ns @ 10 pulse/sec |
| Substrate temperature | 400 – 600°C |
| Total overall growth time (typical) | 120 min. |
| Deposited film thickness (approx.) | 50–500 Å (BN) |

Results from preliminary depositions were mixed. The deposition rate was quite high initially, but then dropped rapidly to zero. Concurrently, a dark rectangular stripe appeared on the surface of the target, corresponding to the shape of the excimer laser cavity. This deactivation was also observed by Doll *et al* [42] when using a KrF laser ($\lambda=248$ nm). It is speculated in the case of ArF that the BN was decomposing

and ablating, which would quickly produce a boron-rich phase that would resist further ablation. By moving the target to an unimpacted region, the deposition could be slowly continued, until after several hours, a layer 200 Å thick was produced. At this point, the target was sufficiently affected to effectively prevent further deposition, and so the substrate was removed for analysis.

X-ray diffraction was performed and a typical spectra is shown in Figure 30. Note that while a number of peaks were observed for hexagonal and wurtzitic BN, no peaks were observed for the cubic phase.

The reason for the lack of the c-BN phase is, at present, unclear though perhaps the higher photon energy of the ArF laser results in processes which are more favorable to the formation of w-BN. Additional x-ray diffraction was performed on the h-BN targets, on both the laser impacted material and the unaffected areas. Figure 31 shows the comparison of these two areas on the target.

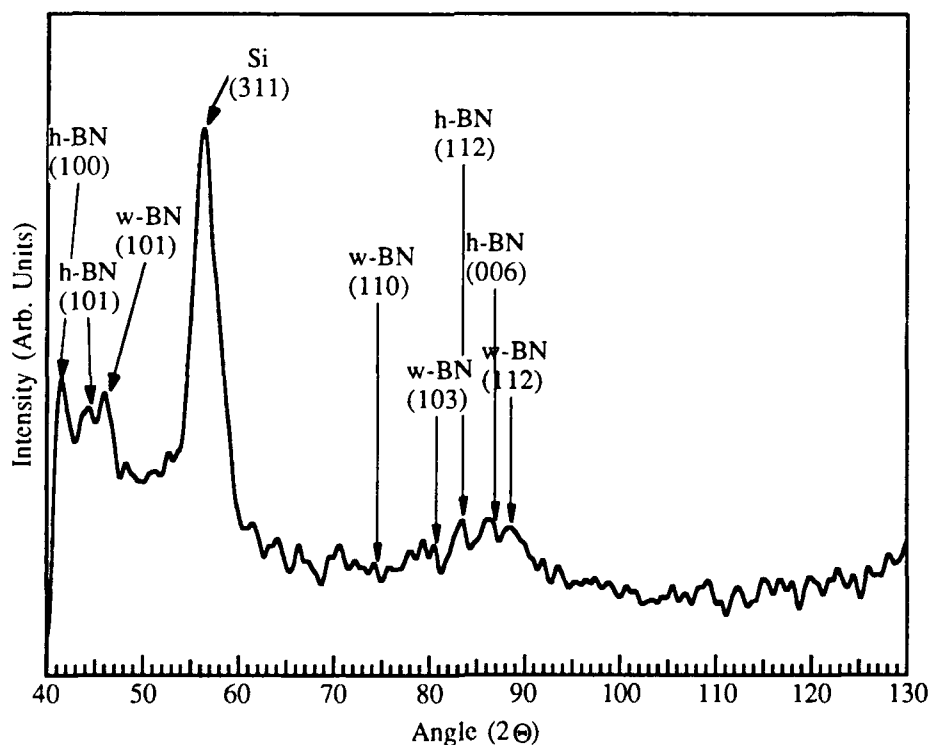


Figure 30. X-ray diffraction spectra ($\text{CuK}\alpha$) of Si (100) target after laser ablation. Film thickness measured during deposition via quartz crystal monitor is 525 Å.

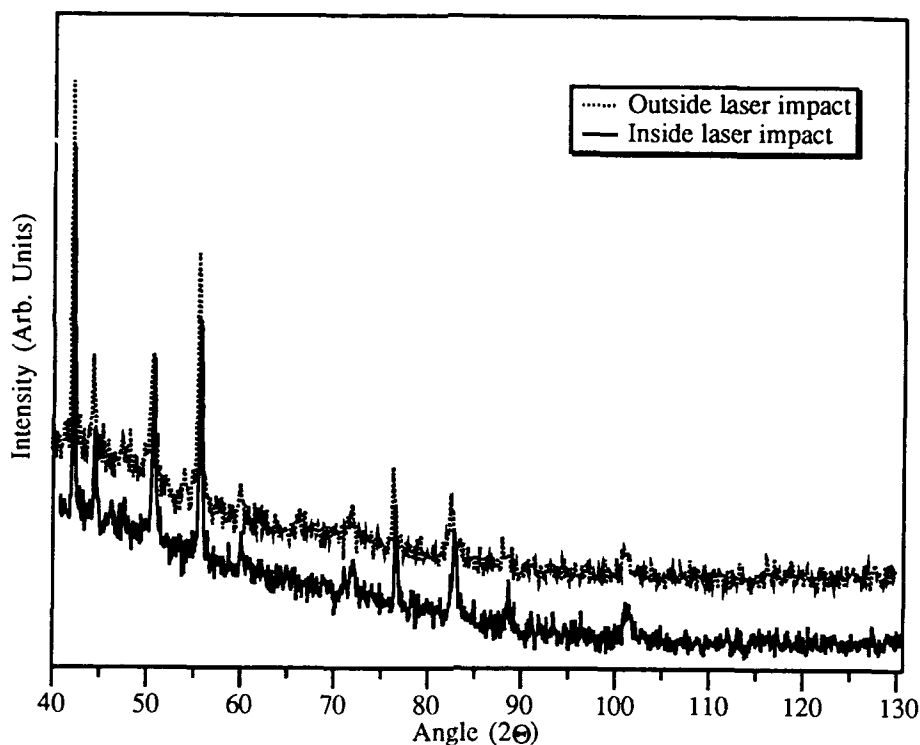


Figure 31. X-ray powder diffraction patterns ($\text{CuK}\alpha$) of hexagonal BN target inside and outside laser ablated area. Diffraction peaks are not indexed since all peaks are from h-BN.

There was no evidence in the diffraction pattern of any residual cubic or wurtzitic BN crystals. Small amounts would be expected and have been observed in other cases [44]. This is true especially, since the laser develops an area which will no longer ablate, and so reduces the energy applied to the target, allowing an intermediate energy input which might convert material without ablating it.

Auger electron spectroscopy showed that a slightly sub-stoichiometric BN layer was deposited on the Si substrate. It also showed a small amount of Ca, which is likely due to impurities in the target, since it was a hot-pressed product and Ca is a typical sintering agent. Surprisingly, AES of the target did not show discernable composition differences between the light (unexposed) and dark (ablated) areas, which were clearly visible in the Auger microscope. Clear differences in the boron peak shape were observed, however. This somewhat anomalous result is under investigation.

VIII. Characterization of Sumitomo c-BN

Work has also been done on the characterization of polycrystalline c-BN substrate materials obtained from Sumitomo Electric in Japan. Figure 32 shows a surface electron energy loss spectroscopy (EELS) plot of the surface of the substrate.

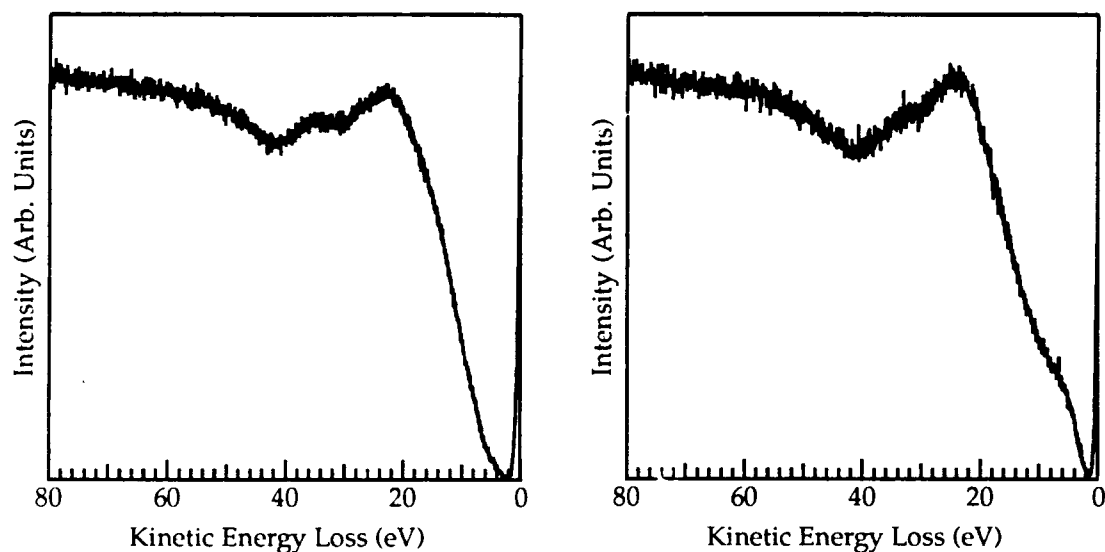


Figure 32. Surface EELS spectra ($E_p=1000$ V) of polycrystalline c-BN sample obtained from Sumitomo Electric Corporation. Left graph shows as received spectra and right graph shows after 3 kV Ar^+ sputter clean followed by $900^\circ C$ anneal.

The plasmon loss features are evident and are similar to spectra taken by transmission EELS done by Hosoi *et al* [45]. The unsputtered spectra on the left shows peaks at 23 and 35 eV. Hosoi *et al* observed a 33 eV feature which was attributed by them to be to a $\sigma \rightarrow \sigma^*$ plasmon transition in w-BN. They observed 25 and 26 eV features which they attributed to $\pi + \sigma$ transitions in amorphous and h-BN. Since our spectra might have been affected by substrate polishing and oxidation or other artifacts from surface treatments, the sample was sputter cleaned and annealed.

The right spectra in Figure 32 shows the plasmon loss features after the annealing. The 33 eV feature is reduced and the 23 eV feature has been shifted up to

26 eV, much closer to the 29 eV peak that Hosoi *et al* observed for the $\sigma \rightarrow \sigma^*$ plasmon transition in c-BN. However, an additional feature has appeared around 9 eV which Hosoi *et al* attributed to a $\pi \rightarrow \pi^*$ plasmon transition in h-BN. Thus, it appears that the sputter clean did remove the most of the surface artifacts, but added a small amount of h-BN. It is not surprising that a relatively low temperature anneal (for BN) of 900°C would be unable to completely reorder the surface. Thus, it appears that spectra of these substrates can then be used as reference standards to characterize the cubic nature of BN films deposited in the MBE system.

One final characterization of the Sumitomo substrates involved examination of the surface via SEM. Shown in Figure 33 is a SEM photograph of the c-BN surface observed in this study.

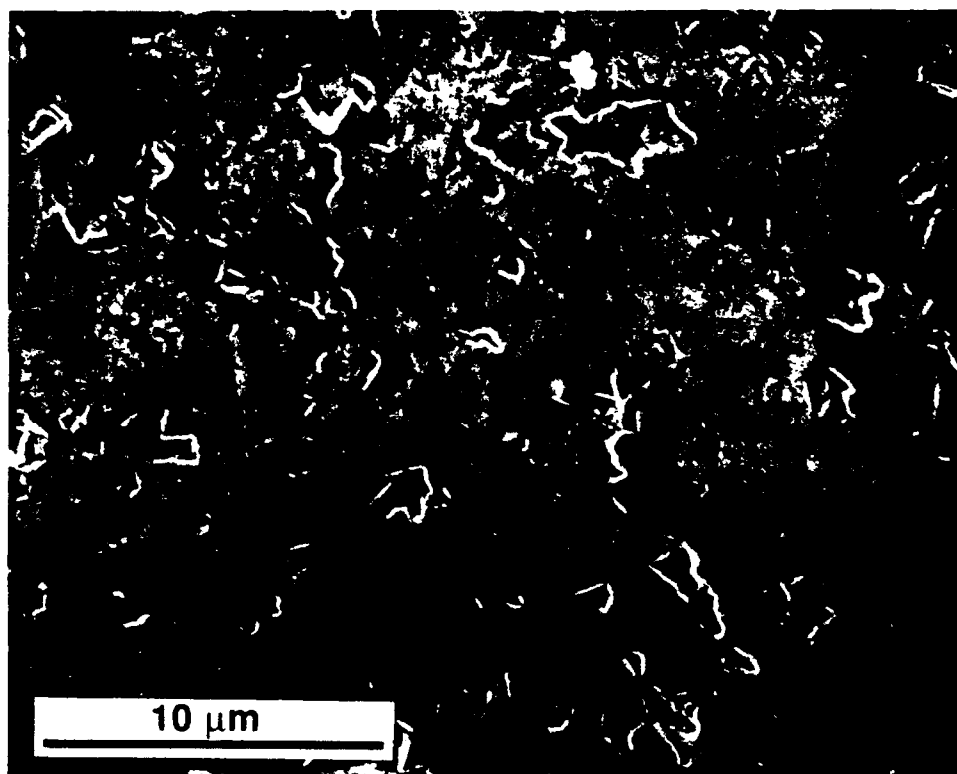


Figure 33. Scanning electron microscope photograph of surface of Sumitomo polycrystalline c-BN substrates.

The surface of the c-BN substrates is quite rough, showing angular pits distributed all over the surface. This is very likely due to the extreme hardness of the c-BN, making polishing without intergranular pullout extremely difficult. It thus remains for future investigation, if these substrates will be appropriate for use in growth studies.

IX. Future Research in the Growth of BN Films

A. Gas Source MBE

Work will continue on various methods of improving the amorphous and microcrystalline nature of the films being deposited. Recent publications [46-49] on growth of c-BN films have indicated that lower substrate temperatures might well be desirable. Lower substrate temperatures will also have lowered surface mobilities of species on the growth surface which would impede proper crystal structure formation. One such method of improving the surface mobility involves use of a high-pressure mercury lamp situated so that it will irradiate the growing film. This type of lamp can excite the boron atom transition at 249.7 nm [50], giving the boron atoms a higher surface mobility, but maintain a lower growth temperature to maintain the cubic structure. This lamp has been purchased and experiments with this modification should begin in the near future.

B. Laser Ablation

Work will also continue on alternate growth technologies for c-BN layers. A new, more powerful excimer laser is in the process of being upfitted into the laboratory where the other ablation experiments have been performed. Before the end of the calendar year, experiments with this new laser will begin, which will provide much higher laser fluences than available with the previous excimer laser.

C. Analytical Techniques

Due to the difficulty of preparing diamond and c-BN samples for examination by TEM, other techniques will need to be heavily relied upon for initial diagnostic information on the crystalline nature and quality of the c-BN films produced. The current x-ray diffractometer has proven to be quite difficult to use with the small single crystal diamond substrates and the resulting oriented films, due to its lack of a goniometer stage.

Work is nearly complete to recommission a diffractometer in the laboratories of Klaus Bachmann, here in the Materials Science and Engineering department at NCSU. This system is a triple crystal diffractometer with a goniometer stage, which will permit accurate alignment of the substrate crystal. Thus, measurement of the individual peaks will be much easier to obtain. In addition, since the x-rays in this system are extremely monochromatic, rocking curves will be possible to measure the strain present in the films.

Further work will also continue in the development of additional techniques for analyzing c-BN films. Further EELS studies will determine how effective that technique will be in observing h-BN and c-BN features. Arrangements have also been made to have further samples analyzed using Raman spectroscopy and/or micro-Raman spectroscopy in the laboratories of Dr. Robert Nemanich in the Physics Department here at NCSU.

IX. References

1. R. F. Davis, Z. Sitar, B. E. Williams, H. S. Kong, H. J. Kim, J. W. Palmour, J. A. Edmond, J. Ryu, J. T. Glass, and C. H. Carter, Jr., *Mat. Sci. & Eng. B* **1**, 77 (1988).
2. P. M. Dryburgh, *J. Cr. Growth* **94**, 23 (1989).
3. Y. Koide, H. Itoh, M. R. H. Khan, K. Hiramatu, N. Sawaki, and I. Akasaki, *J. Appl. Phys.* **61**, 4540 (1987).
4. W. T. Tsang, *Appl. Phys. Lett.* **39**, 786 (1981).

5. M. G. Burt, *Electron. Lett.* **19**, 210 (1983).
6. P. Davson, G. Duggan, H. I. Ralph, and K. Woodbridge, *Superlattices and Microstr.* **1**, 173 (1985).
7. N. Holonyak, Jr., R. M. Kolbas, R. D. Dupuis, and P. D. Dapkus, *IEEE J. Quantum Electron.* **QE 16**, 170 (1980).
8. Z. Sitar, M. J. Paisley, D. K. Smith, and R. F. Davis, *Rev. Sci. Instr.* **61**, 2407 (1990).
9. J. C. Bravman and R. Sinclair, *J. Electron Microsc. Tech.* **1**, 53 (1987).
10. J. W. Matthews and A. E. Blakeslee, *J. Cryst. Growth* **27**, 118 (1974).
11. For example; R. L. Liboff, *Introductory Quantum Mechanics*, Holden-Day, Inc., San Francisco (1980).
12. *Landoldt-Börnstein New Series*, Vol. III/17d, Springer-Verlag Berlin, Heidelberg, New York, Tokyo (1982).
13. N. G. Anderson, *Ph. D. Thesis*, North Carolina State University, Dept. of El. and Comp. Eng. (1988).
14. K. Das and D. K. Ferry, *Solid-State Electron.* **19**, 851 (1976).
15. J. I. Pankove, *Mat. Res. Soc. Proc.* **97**, 409, Materials Research Society 1987.
16. J. I. Pankove, *Mat. Res. Soc. Proc.* **162**, 515, Materials Research Society 1990.
17. W. Seifert and A. Tempel, *Phys Stat. Sol. A* **23**, K39 (1974).
18. M. Mizuta, S. Fujieda, Y. Matsumoto, and T. Kawamura, *Jap. J. Appl. Phys.* **25**, L945 (1986).
19. M. J. Paisley, Z. Sitar, J. B. Posthill, and R. F. Davis, *J. Vac. Sci. Technol. A* **7**, 701 (1989).
20. T. P. Humphreys, C. A. Sukow, R. J. Nemanich, J. B. Posthill, R. A. Rudder, S. V. Hattangady and R. J. Markunas, *Mat. Res. Soc. Proc.* **162**, 531, Materials Research Society 1990.
21. R. C. Powell, G. A. Tomasch, Y. W. Kim, J. A. Thornton and J. E. Greene, *Mat. Res. Soc. Proc.* **162**, 525, Materials Research Society 1990.
22. H. Morkoc, private communication.
23. J. I. Pankove, *J. Luminescence* **7**, 114 (1973).
24. J. I. Pankove, and S. Bloom, *RCA Rev.* **36**, 163 (1975).

25. R. F. Davis, Z. Sitar, and M. J. Paisley, Annual Progress Report, NTIS Ref. No. ADA210380.
26. Z. Sitar, M. J. Paisley, D. K. Smith, and R. F. Davis, *Rev. Sci. Instr.* **61**, 2407 (1990).
27. See for example: J. I. Pankove, *Optical Processes in Semiconductors*, Dover Publications, Inc., New York (1971).
28. D. D. Manchom, A. S. Barker, P. J. Dean and R. B. Zetterstrom, *Solid State Commun.* **8**, 1227 (1970).
29. R. F. Davis, Z. Sitar, B. E. Williams, H. S. Kong, H. J. Kim, J. W. Palmour, J. A. Edmond, J. Ryu, J. T. Glass, and C. H. Carter, Jr., *Mat. Sci. & Eng. B* **1**, 77 (1988).
30. J. I. Pankove, *Mat. Res. Soc. Proc.* **162**, 515, Materials Research Society 1990.
31. H. Amano, M. Kito, K. Hiramatsu and I. Akasaki, *Proc. 16th Int. Symp. on Gallium Arsenide and Related Compounds*, Karuizawa, Japan (1989).
32. H. Amano, M. Kito, K. Hiramatsu and I. Akasaki, *Jap. J. Appl. Phys.* **28**, L2112 (1989).
33. H. Amano, I. Akasaki, T. Kozawa, K. Hiramatsu, N. Sawaki, K. Ikeda and J. Ishii, *J. Lumin.* **40 & 41**, 121 (1988).
34. Z. Sitar, M. J. Paisley, D. K. Smith, and R. F. Davis, *Rev. Sci. Instr.* **61**, 2407 (1990).
35. Z. Sitar, M. J. Paisley, B. Yan, J. Ruan, J. W. Choyke and R. F. Davis, *J. Vac. Sci. Technol. B* **8**, 316 (1990).
36. R. C. DeVries, *Cubic Boron Nitride: Handbook of Properties*, Technical Information Series, General Electric Company, Corporate Research and Development, 72CRD178, 1972.
37. M. J. Paisley, Z. Sitar, J. B. Posthill, and R. F. Davis, *J. Vac. Sci. Technol. A* **7**(3), 701 (1989).
38. M. J. Paisley, Z. Sitar, C. H. Carter Jr., and R. F. Davis, in *SPIE's OE/LASE—Innovative Science and Technology Symposium* C. A. Kukkonen, Eds. (SPIE—The International Society for Optical Engineering, Los Angeles, CA, 1988), pp. 8.
39. M. J. Paisley, Z. Sitar, B. Yan, and R. F. Davis, *J. Vac. Sci. Technol. B* **8**(2), 323 (1990).
40. J. C. Bravman, and R. Sinclair, *J. Electron Microsc. Technique* **1**, 53 (1984).
41. J. F. Prins, *J. Phys. D* **22**, 1562 (1989).

42. G. L. Doll, J. A. Sell, L. Salamanca-Riba, and A. K. Ballal, in *Spring 1990 Meeting of the Materials Research Society* J. T. Glass, Eds. Boston, MA, 1990.
43. D. R. Clarke, and F. Adar, in *Advances in Materials Characterization* D. R. Rossington, R. A. Condrate, and R. L. Snyder, Eds. (Plenum Press, Alfred University, 1982), pp. 199.
44. M. Sokolowski, A. Sokolowska, M. Wronikowski, and T. Kosik, *J. Mater. Sci.* **25**(1a), 263 (1990).
45. J. Hosoi, T. Oikawa, M. Inoue, Y. Matsui, and T. Endo, *J. Electron Spectros. Relat. Phenom.* **27**, 243 (1982).
46. M. Okamoto, H. Yokoyama, and Y. Osaka, *Jpn. J. Appl. Phys.* **29**(5), 930 (1990).
47. J. Kouvetakis, V. V. Patel, C. W. Miller, and D. B. Beach, *J. Vac. Sci. Technol. A* **8**(6), 3929 (1990).
48. T. Ikeda, Y. Kawate, and Y. Hirai, *J. Vac. Sci. Technol. A* **8**(4), 3168 (1990).
49. K. H. Seidel, K. Reichelt, W. Schaal, and H. Dimigen, *Thin Solid Films* **151**(2), 243 (1987).
50. H. L. Anderson, Ed., *A Physicist's Desk Reference* (American Institute of Physics, New York, 1989).